

SURVEY OBSERVATION OF CH₃NH₂ AND ITS FORMATION PROCESS

TAIKI SUZUKI,^{1,2} LITON MAJUMDAR,³ KAZUKI TOKUDA,⁴ HARUMI MINAMOTO,⁵ MASATOSHI OHISHI,² MASAO SAITO,²
TOMOYA HIROTA,² HIDEKO NOMURA,^{5,2} AND YOKO OYA⁶

¹*Astrobiology Center, Osawa 2-21-1, Mitaka, Tokyo 181-8588, Japan*

²*National Astronomical Observatory of Japan, Osawa 2-21-1, Mitaka, Tokyo 181-8588, Japan*

³*School of Earth and Planetary Sciences, National Institute of Science Education and Research, HBNI, Jatni 752050, Odisha, India*

⁴*Department of Physical Science, Graduate School of Science, Osaka Prefecture University, 1-1 Gakuen-cho, Naka-ku, Sakai, Osaka 599-8531, Japan*

⁵*Department of Earth and Planetary Sciences, Tokyo Institute of Technology, 2-12-1 Ookayama, Meguro-ku, Tokyo, 152-8551, Japan*

⁶*Department of Physics, The University of Tokyo, 7-3-1, Hongo, Bunkyo-ku, Tokyo 113-0033, Japan*

(Received September 20, 2021; Revised; Accepted)

Submitted to ApJ

ABSTRACT

We present the observational result of a glycine precursor, methylamine (CH₃NH₂), together with methanol (CH₃OH) and methanimine (CH₂NH) towards high-mass star-forming regions, NGC6334I, G10.47+0.03, G31.41+0.3, and W51 e1/e2 using ALMA. The molecular abundances toward these sources were derived using the rotational diagram method and compared with our state-of-the-art chemical model. We found that the observed ratio of “CH₃NH₂/CH₃OH” is in between 0.11 and 2.2. We also found that the observed “CH₃NH₂/CH₃OH” ratio agrees well with our chemical model by considering the formation of CH₃NH₂ on the grain surface via hydrogenation process to HCN. This result clearly shows the importance of hydrogenation processes to form CH₃NH₂. NGC6334I MM3, where CH₃NH₂ was not detected in this study and showed “CH₃NH₂/CH₃OH” ratio of less than 0.02, is clearly distinguished from the other cores.

Keywords: astrochemistry-methods: observational-ISM: abundances-ISM: molecules

taiki.suzuki@nao.ac.jp

liton@niser.ac.in

liton.majumdar@jpl.nasa.gov

1. INTRODUCTION

It is believed that the first chemical evolution toward the origin of life would have started in molecular clouds and continued within the protoplanetary disk, followed by their delivery to the early Earth by comets and asteroids. However, the synthesis and evolution of organic molecules, which form the building blocks of more complex biotic molecules, is not well understood. Over the last several years, there have been significant advances in this field thanks to dedicated searches for molecules of biological importance in the ISM and in the atmospheres of comets. Among them, observations in the direction of the Galactic center towards Sgr B2(N) with the Green Bank Telescope (GBT) have led to the detections of interstellar aldehydes, namely propenal (CH_2CHCHO) and propanal ($\text{CH}_3\text{CH}_2\text{CHO}$) (Hollis et al. 2004a) and simple aldehyde sugars like glycoaldehyde (CH_2OHCHO) (Hollis et al. 2004b), the first keto ring molecule to be found in the ISM. Recently, propylene oxide ($\text{CH}_3\text{CHCH}_2\text{O}$) (McGuire et al. 2016) has also been detected in the same source. This is the first molecule detected in interstellar space that has the property of chirality, making it a leap forward in our understanding of how prebiotic molecules are made in the Universe. In the era of the Atacama Large Millimeter Array (ALMA), the detection of the branched alkyl molecule iso-propyl cyanide ($i\text{-C}_3\text{H}_7\text{CN}$) in Sgr B2(N) also gave us the clues to the presence of amino acids in the ISM due to its key side-chain structure (Bellocche et al. 2014). The amino acids are the building blocks of life and this is why the search for amino acids and their complex organic precursors at different stages of star and planet formation is one of the exciting topics in modern astronomy. Since glycine is the simplest amino acid and the only non-chiral member out of 20 standard amino acids, it has gathered attention of researchers. Recently, volatile glycine ($\text{NH}_2\text{CH}_2\text{COOH}$) was detected in the coma of comet 67P/Churyumov-Gerasimenko by the ROSINA (Rosetta Orbiter Spectrometer for Ion and Neutral Analysis) mass spectrometer (Altwegg et al. 2016), supporting glycine’s interstellar origin.

Revealing the formation pathways to glycine is important topic for astrochemistry and astrobiology, since most of the prebiotic molecules contain N atoms and the general chemical evolution of N-bearing molecules in the ISM is poorly known. The high-mass star-forming regions are the best sources to study the chemical evolution of COMs (Complex Organic Molecules) with their high gas density and the warm environment that trigger the molecular evolution through thermal hopping of molecules on grains. In this context, formation processes to glycine in the high-mass star-forming regions have been studied by many authors: [I] It is suggested that protonated hydroxylamine (NH_2OH^+) will react with acetic acid (CH_3COOH) in the gas phase Blagojevic et al. (2003) to form glycine. [II] The importance of grain surface chemistry is emphasized as well. CH_3NH_2 will react with CO_2 to form glycine under the radiation of UV photons or cosmic rays Holtom et al. (2005); Lee et al. (2009). [III] Singh et al. (2013) suggested that glycine can be formed via successive gas phase radical-radical, radical-molecule reactions of simple species, such as CH_2 , NH_2 , CH , and CO . Of the precursors of glycine, recent works have improved the understanding of CH_3NH_2 chemistry. Experimentally, Kim & Kaiser (2011) reported the formation of CH_3NH_2 after electron and photon irradiation on interstellar ice analogues consisting of CH_4 and NH_3 . This path would involve the recombination of radical species, CH_3 and NH_2 ($\text{CH}_3 + \text{NH}_2 \rightarrow \text{CH}_3\text{NH}_2$), which are the products of decomposition of CH_4 and NH_3 . Another candidate pathway would be a successive hydrogenation processes to HCN ($\text{HCN} + 2\text{H} \rightarrow \text{CH}_2\text{NH}$, and $\text{CH}_2\text{NH} + 2\text{H} \rightarrow \text{CH}_3\text{NH}_2$) (Woon 2002). Theule et al. (2011) experimentally demonstrated this formation process using the interstellar ice analogues containing HCN.

The study of the chemical model, where the evolution of molecular abundances are numerically solved with thousands of reactions along with the physical evolution of the star, is an essential tool to test the importance of formation paths. The formation processes of glycine’s precursors have been discussed with the chemical model studies. Garrod (2013) has compared several possible processes to form glycine, including both gas phase and grain surface reactions and suggested that with a model for high-mass star-forming region (fast warm-up model), glycine is most efficiently formed via the reaction between CH_2NH_2 and COOH radicals, where COOH radical is formed from the destruction of HCOOH . Suzuki et al. (2018) extended this work and suggested the acceleration of glycine formation by the photochemical reactions of CH_3NH_2 and CO_2 , which was supported by experiments (Lee et al. 2009). In either cases, CH_3NH_2 may play an important role in the formation of glycine. The detections of CH_3NH_2 in Murchison meteorite and coma of comet 67P/Churyumov-Gerasimenko suggest the formation of CH_3NH_2 in the extra terrestrial condition (Pizzarello et al. 1994; Altwegg et al. 2016). Altwegg et al. (2016) has pointed out this chemical link considering the co-existence of glycine and CH_3NH_2 in the coma of comet 67 P as well. With the chemical model, Suzuki et al. (2016) showed that CH_3NH_2 is formed on grains via the successive hydrogenation processes to HCN and CH_2NH , which agrees with previous terrestrial studies (Theule et al. 2011). On the other hand, we got an unexpected result that the

grain surface chemistry to CH₂NH is less important to explain the gas phase CH₂NH due to its rapid conversion to CH₃NH₂ on grains. Instead, CH₂NH is efficiently formed via a gas phase reaction of “CH₃ + NH → CH₂NH + H”.

Such theoretically predicted formation processes must be confirmed by the observation toward actual star-forming regions. The number of studies for glycine precursors is very small for the low-mass star-forming regions. CH₂NH is also detected toward a Solar-Like protostar, IRAS16293-2422B, as a part of ALMA-PILS project (Ligterink et al. 2018), and toward the molecular cloud L183 and the translucent cloud CB17 as well (Turner 1999). However, they could not detect CH₃NH₂ and currently the detection of CH₃NH₂ is not achieved toward low-mass star-forming regions.

On the other hand, the detections of glycine’s precursors toward high-mass star-forming regions have been achieved by many authors. So far, many authors claimed the detection of CH₂NH toward Sgr B2 region. This molecule is detected toward Sgr B2(OH) (Godfrey et al. 1973; Turner 1989), Sgr B2(N) (Halfen et al. 2013), and Sgr B2(M) (Sutton et al. 1991). Nummelin et al. (1998) also successfully detect it in Sgr B2(N), (M), and (NW). Jones et al. (2008, 2011) found the distribution of CH₂NH from Sgr B2(N) to (S) at 3 mm and 7 mm with the MOPRA telescope. CH₂NH is reported toward other high-mass star-forming regions, W51 e1/e2, Orion KL, and G34.3+0.15 (Dickens et al. 1997; White et al. 2003), and G19.61-0.23 (Qin et al. 2010). We extended CH₂NH survey and reported new detections of CH₂NH toward G10.47+0.03, G31.41+0.3, NGC6334F, and DR21(OH) (Suzuki et al. 2016). NGC6334F is also referred as NGC6334I and hereafter we use the term of NGC6334I to avoid confusion with the works by other authors. Widicus Weaver et al. (2017) added new CH₂NH sources of GCM+0.693-0.027, the shocked region located in the Sgr B2 complex, a massive hot core G12.91-0.26, and G24.33+00.11 MM1. CH₃NH₂ was reported early toward Sgr B2 (Kaifu et al. 1974; Fourikis et al. 1974), and Belloche et al. (2013) presented the detailed analysis toward Sgr B2 (N) and (M) with IRAM 30 m telescope. Halfen et al. (2013) showed that CH₂NH and CH₃NH₂ toward Sgr B2 (N) have the different excitation temperatures, 44±13 and 159 ±30 K, respectively, suggesting that they exist in the different environment. Though the survey observation toward other high-mass star-forming regions by Ligterink et al. (2015) could not confirm CH₃NH₂, Ohishi et al. (2019) succeeded the detection of CH₃NH₂ toward G10.47+0.03 with NRO 45m telescope. Since the rotation temperature of CH₃NH₂ was less than 45 K, the observed CH₃NH₂ would be in the cold envelope surrounding the hot core. After that, Bøgelund et al. (2019) confirmed the detection of CH₃NH₂ in NGC6334I, resolving three clumps called MM1, MM2, and MM3. Furthermore, tentative detection of CH₃NH₂ were reported toward Orion Hot core (Pagani et al. 2017). Since glycine’s precursors are well known in the high-mass star-forming regions, it is possible to discuss their formation paths with chemical model using the typical abundance of these species.

Since CH₃OH is the most abundant complex organic molecules in the star-forming regions, it will be helpful to understand the chemical evolution of CH₃NH₂. CH₃OH is known to be formed via the hydrogenation process to CO (CO + 2H → H₂CO, and H₂CO + 2H → CH₃OH), which is very similar to the predicted formation path of CH₃NH₂ (HCN + 2H → CH₂NH, and CH₂NH + 2H → CH₃NH₂). Therefore the comparison of the column densities between CH₃NH₂ and CH₃OH would be useful to reveal the formation process of CH₃NH₂. Since the molecular surveys of CH₃NH₂, CH₂NH, and CH₃OH have been mainly performed with single dish telescope, the column density ratio utilizing such single dish data will suffer from the unknown source sizes that lead to the different degree of the beam dilution. Therefore, the interferometric observations of these species are strongly desired. In this paper, we will report the observations of CH₃NH₂, CH₂NH, and CH₃OH toward G10.47+0.03, NGC6334I, G31.41+0.3, and W51 e1/e2 region by ALMA telescope. The detail of our observation is described in Section 2. The observational result is presented in Section 3. Our result is compared with the chemical model in Section 4. We summarize our work in Section 5.

2. OBSERVATION AND ANALYSIS

2.1. Source Selection

We selected high-mass star-forming regions where we have already detected CH₂NH with NRO 45m telescope (Suzuki et al. 2016). In this work, we performed a survey observation of the glycine precursor, CH₂NH, toward CH₃OH-rich high-mass star-forming regions. As a result, we detected CH₂NH toward eight sources. One finding of our work was that CH₂NH showed wide range of fractional abundances among our sources. Since CH₂NH-rich sources showed the different strength of a recombination line, H54β, the different abundance of CH₂NH may be due to the different evolutionary phase. Therefore, we selected four sources, NGC6334I, G10.47+0.03, G31.41+0.3, and W51 e1/e2, from Suzuki et al. (2016), so that we can cover the different evolutionary phase of the star-formation.

Their coordinates, the source velocities, the distances, and previously reported CH₂NH fractional abundances are summarized in Table 1.

2.2. Spectroscopy

The molecular line parameters of CH₃OH, CH₃NH₂, and CH₂NH are provided by the database of SLAIM from the on-line database splatalogue¹. The quantum number of CH₃OH transitions are described by J , $\pm K_a$, and Γ . For transitions with $\Gamma = A$, the Γ is associated with a '+' or '-' sign to represent the parity. On the other hand, $\Gamma = E_1$ and E_2 are presented by the identical alphabet of $\Gamma = E$, but denoted by the positive and negative sign of K , respectively, due to the absence of a parity entry. CH₂NH is a simple asymmetric top with all atoms being on the simple plane, and the transitions are described using labels J , K_a , and K_c . The transitions of CH₃NH₂ are labeled by the torsion-inversion rotation irreducible representations Γ , with its states of labeled with the A_1 , A_2 , B_1 , B_2 , $E_{1\pm 1}$, and $E_{2\pm 1}$ (Ilyushin et al. 2007). The selection rules are $\Gamma = A_1 \leftrightarrow A_2$, $B_1 \leftrightarrow B_2$, $E_{1\pm 1} \leftrightarrow E_{1\pm 1}$, and $E_{2\pm 1} \leftrightarrow E_{2\pm 1}$. The symmetry levels have nuclear spin-statistical weights of 1 for the A_1 , A_2 , and E_2 states and 3 for the B_1 , B_2 , and E_1 components. The hyper fine structures of CH₂NH and CH₃NH₂ are not considered in this analysis.

2.3. Observation

Our observations were carried out with ALMA cycle 5 in May, 2018, using the ALMA Band 5 and 6 receivers. This interferometric observations have the advantage to obtain the spatial distributions of molecules. Although we could not get the source size by our previous single dish observation, the information of the source size are essential to discuss the accurate column densities. The observing parameters, such as the phase centers, the spectral resolutions, the maximum recoverable scales, and the angular resolutions, are summarized in Tables 2 and 3. The observed frequency ranges are the same for all sources, as the center frequencies, the band widths and number of channels are summarized in Table 4. These receiver setups were designed to cover the number of molecular transitions of CH₃OH, CH₃NH₂, and CH₂NH that can cover the wide range of the upper state energy level (Table 5). With the on-line database splatalogue, we excluded the possibility of the contamination by other strong molecular lines for these transitions.

2.4. Analysis

Our data were calibrated by Common Astronomy Software Applications (CASA) V.5.1.1, with the ALMA Cycle 5 pipeline. For the subtraction of the continuum emission in the (u, v) domain (the raw visibilities measured by the interferometer), we determine the continuum levels statistically using the method described in Sanchez-Monge et al. (2018). First, the spectra before the continuum subtraction is obtained. Second, the histograms of the intensity are created using the all channels in the spectra. Finally, we perform the Gaussian fitting to the lowest peak in the histogram to obtain the peak, the mean and the standard deviation of the Gaussian. As an example, we shown the histogram of the intensity and the result of the Gaussian fitting in Figure 1. The continuum level is determined as the mean value of the Gaussian. We regarded the channels with the intensity less than three-sigma level from the continuum level, and the CASA task UVCONTSUB is used to subtract the continuum emission.

Then, the deconvolved image was obtained by the CASA task TCLEAN by applying natural weighting. Prior to the detailed analysis of molecular abundance, we created the moment 0 map of the intensity through the CASA task IMMOMENT. The distribution of the integrated intensities for “4, 1, $E \rightarrow 3, 1, E$ ” transition of CH₃OH, “4, 1, $E_{1+1} \rightarrow 3, 0, E_{1+1}$ ” transition of CH₃NH₂, and “3, 2, 2 $\rightarrow 2, 2, 1$ ” transition of CH₂NH, were as shown through Figures 2 to 5. These lines are less likely to be contaminated by other transitions and detected toward all sources. The upper energy levels and the products of the intrinsic intensity and the square of the permanent dipole moments of these transitions are, 44.3, 44.9, and 25.9 K, and 3.1, 2.9, and 3.7 D². If we use the analysis result described in Section 3, CH₃OH “4, 1, $E \rightarrow 3, 1, E$ ” transition shows the relatively high optical thickness of 1.1 in NGC 6334I MM1, but less than 0.6 for the other sources. The optical depths of “4, 1, $E_{1+1} \rightarrow 3, 0, E_{1+1}$ ” transition of CH₃NH₂, and “3, 2, 2 $\rightarrow 2, 2, 1$ ” transitions are less than 0.3 for all sources. Hence they would trace the warm and somewhat dense regions.

3. RESULT

3.1. Spatial Distribution

¹ <http://www.cv.nrao.edu/php/splat/>

Figure 2 presents the integrated intensity maps of CH₃OH 4, 1, $E \rightarrow 3, 1, E$, CH₃NH₂ 4, 1, $E_{1+1} \rightarrow 3, 0, E_{1+1}$, and CH₂NH 3, 2, $2 \rightarrow 2, 2, 1$ transitions toward NGC6334I. Hunter et al. (2006) performed the mapping observation of 1.3 mm continuum emission with Submillimeter Array (SMA), and reported the structures named SMA1, SMA2, SMA3, and SMA4. Later, with Karl G. Jansky Very Large Array (VLA) and ALMA, Brogan et al. (2016) carried out the high angular resolution mapping as high as 0.''17 (220 AU) from 5 cm to 1.3 mm. They found the MM1, MM2, MM3, MM4, MM6, MM7, MM9, and CM2, where MM1, MM2, MM3, and MM4 are respectively corresponding to previously known SMA1, SMA2, SMA3, and SMA4. Of these components, MM3 is known as an UCHII region associated with free-free emission (Hunter et al. 2006). Many organic molecules have been reported toward MM1 and MM2 (e.g., Walsh et al. 2010; Zernicke et al. 2012). The molecular distribution overlap with the positions of MM1, MM2, and MM3. In our observation, CH₃OH clearly showed extended distribution than CH₃NH₂ and CH₂NH. The CH₃OH distribution is complex with its size of ~ 5 and ~ 3 '' , respectively for MM1 and MM2, but ~ 10 '' if we consider the whole emission including the southern weak emission. This whole distribution is close to the maximum recoverable scale. CH₃NH₂ and CH₂NH emissions are dominant from MM1, with their source sizes of ~ 3 and ~ 2 '' , respectively. Though CH₃NH₂ and CH₂NH emissions in MM2 are weaker than MM1, there are compact (~ 1 '') sources. Though the previous continuum mapping observation by Brogan et al. (2016) suggested the existence of at least seven and two unresolved cores in MM1 and MM2, respectively, our spatial distribution is not sufficient to resolve such structures. Future high-resolution mapping observations of CH₃OH would resolve the distribution of CH₃OH and probably CH₃NH₂ and CH₂NH inside MM1 and MM2. The distributions of CH₃NH₂ and CH₂NH have already been reported by Bøgelund et al. (2019) toward MM1 and MM2 with the different frequency, which agree with our results. In NG6334I region, we extracted the spectra from the peak positions of the CH₂NH intensity in MM1 region, since the distribution of CH₂NH is compact. The coordinate of NGC6334I MM1 is offsetted from the observed position of Bøgelund et al. (2019) by about 2''. The MM2 position is selected as the peak intensity position of CH₃NH₂, which is very close to the MM2 region analyzed in Bøgelund et al. (2019) and the peak intensity of the continuum. The MM3 position is selected as the peak intensity position of CH₃OH since both CH₂NH and CH₃NH₂ intensities are so weak. Our MM3 coordinate is offsetted toward north by about 3'' than Bøgelund et al. (2019).

G10.47+0.03 is a well known massive star-forming region associated with UCHII and two HCHII regions. In our mapping region, UCHII regions, A, B, and C, are known through the 2 and 6 cm mapping by VLA (Wood & Churchwell 1989). The high resolution mapping observation at 1.3 cm with VLA further resolved the component B into HCHII regions B1 and B2, and interpreted this source as face-on rotating disks (Cesaroni et al. 1998). They showed the absorption of the NH₃ (4,4) transition toward these B1 and B2 cores, probably due to the molecular outflow originating from HCHII regions. The component D was detected with 3.6 cm continuum emission (Cesaroni et al. 2010), while other components A, B1, B2 were resolved with 6, 2, and 1.3 cm continuum as well. Cesaroni et al. (2010) also provided the evidence of the infalling gas toward the embedded cores associated with the outflow. While these components are not resolved in Figure 3 with our low spatial resolution, the extension of CH₃OH transition toward north indicate that component D only show CH₃OH not being associated with CH₃NH₂ and CH₂NH. Other spatial structures are not resolved even with the other transitions of CH₃OH, CH₃NH₂, and CH₂NH. Since the southern component is not reported by Cesaroni et al. (2010), this feature may be due to very young source where continuum emission is so weak. These components are depicted on our integrated intensity maps in Figure 3. The source size is ~ 3 '' for CH₃OH, while they are ~ 2 '' for CH₃NH₂ and CH₂NH. The distribution of CH₃OH is slightly elongated toward north than CH₃NH₂ and CH₂NH, suggesting that CH₃OH is also abundant in cores A and D. On the other hand, the distribution of CH₃NH₂ and CH₂NH would be limited to B1 and B2, though our data cannot distinguish these cores. The spectra in G10.47+0.03 was extracted from the peak intensity position of CH₃NH₂, which is corresponding to the B1 and B2 positions.

G31.41+0.3 is a massive star-forming region similar to G10.47+0.03. Although this source is known to have UCHII region, the position of hot molecular core is away from the UCHII region by about 5'' (Cesaroni et al. 1994), which is the outside of Figure 4. Cesaroni et al. (2010) detected weak continuum sources A and B inside the hot molecular core of G31.41+0.3. These continuum emissions are thought to be originated from the thermal jet rather than UCHII regions. The non-detection of UCHII region inside of G31.41+0.3 implies that this source is less evolved than G10.47+0.03 (Cesaroni et al. 2010). Our peak positions agree with the position of previously known hot molecular core. The source size is ~ 4 '' for CH₃OH, while they are ~ 2 '' for CH₃NH₂ and CH₂NH. The positions of sources A and B are shown on our integrated intensity maps in Figure 4. These sources are too close to be distinguished with each core with our spatial resolution. The detailed spatial structure of this source is not resolved even with the other transitions

of CH₃OH, CH₃NH₂, and CH₂NH. We extracted the spectra from the peak intensity position of CH₃NH₂, which is almost the identical to sources A and B.

W51 e1/e2 region is the well known protocluster region, which possess UCHII regions e1, e2, e3, e4, and e8 in our mapping regions (Gaume et al. 1993; Zhang & Ho 1997). These structures are shown on our integrated intensity maps (Figure 5). The emission peaks coincide with e2 and e8 components. Through the mapping observation of 870 μ m dust continuum emission with SMA, Tang et al. (2009) detected the extension of dust ridge toward northwest of e2 with an overall length of $\sim 2''$, and southwest of e8 with an overall length of $\sim 3''$, probably being controlled by magnetic field. The southwest distribution of CH₃OH from e8 are clearly seen in our map, overlapping with the above dust ridge. The characteristic northwest distribution of CH₂NH from e2 traces another dust ridge. W51 e2 is the strongest HII region which is thought to be powered by O8-type star (Shi et al. 2010). Shi et al. (2010) performed continuum mapping observation toward W51 e2 at 0.85 and 1.3 mm with VLA, and 7 and 13 mm with ALMA. They identified sub cores named e2-N, e2-W, e2-E, and e2-NW. Only the emission from e2-N are thought to be free-free emission from the HII region, while the other continuum emission would be from dust. Of four sources, e2-E is the only source being associated with the the hydrogen recombination lines. Goddi et al. (2016) found that e2-E and e2-NW are associated with NH₃ and CH₃OH emissions, while e2-W is traced by the absorption. These detailed structure in e2 is not resolved in our maps.. The transitions of CH₃OH 4, 1, $E \rightarrow 3, 1, E$, CH₃NH₂ 4, 1, $E_{1+1} \rightarrow 3, 0, E_{1+1}$, and CH₂NH 3, 2, $2 \rightarrow 2, 2, 1$ distribute toward both e2 and e8. The source size is $\sim 3''$ for CH₃OH, while they are $\sim 2''$ for CH₃NH₂ and CH₂NH for e2, while they are $\sim 3, \sim 1, \text{ and } \sim 2''$, respectively, for CH₃OH, CH₃NH₂, and CH₂NH, in e8. These distributions are consistent with the other transitions of CH₃OH, CH₃NH₂, and CH₂NH. We extracted the spectra from the peak positions of CH₃NH₂ intensity, which are corresponding to W51 e2-E and e8, and hereafter we call W51 e2-E as simply W51 e2.

In total, molecular abundances of CH₃OH, CH₃NH₂, CH₂NH were examined toward seven cores as summarized in Table 7.

3.2. Spectra and Analysis

All the molecular lines used in our analysis are shown through Figures 7 to 13. We note that the rest frequencies of CH₂NH 7, 1, $6 \rightarrow 7, 0, 7$ transition at 250.16168 GHz and CH₃NH₂ 2, 2, $B_2 \rightarrow 2, 1, B_1$ transition at 250.1594 GHz are blended with each other. Since the rest frequencies of these transitions are separated by 2.2 MHz, we assigned the transitions using the peak frequency obtained from the Gaussian fitting.

Some line shapes observed toward NGC6334I MM1 are not well fitted by Gaussian. This would be due to the subcomponents in this source which are not resolved with our spatial resolution. For other sources, molecular lines are relatively well fitted by Gaussian, though some transitions are suffering from the contamination by other molecular lines. In this case, least-squares fitting is performed assuming two components of Gaussian. The rest frequencies of transitions calculated from the source velocities are presented by the dotted lines.

The FWHM line widths and the peak values are obtained through the Gaussian fitting. The detected lines are shown through Tables 7 to 13 with their line parameters. While CH₃OH and CH₂NH are detected toward all sources, CH₃NH₂ is not confirmed toward NGC6334I MM3. We calculated column densities using the rotation-diagram method described in Turner (1991), and the following equation is employed:

$$\log \frac{3kW}{8\pi^3\nu S\mu^2 g_{\text{I}} g_{\text{K}}} = \log \frac{N}{Q_{\text{rot}}} - \frac{E_{\text{u}}}{k} \frac{\log e}{T_{\text{rot}}} \quad (1)$$

where W is the integrated intensity, S is the intrinsic line strength, μ is the permanent electric dipole moment, g_{I} and g_{K} are the nuclear spin degeneracy and the K -level degeneracy, respectively, N is the column density, Q_{rot} is the rotational partition function, E_{u} is the upper level energy, and T_{rot} is the rotation temperature. The rotation diagrams for all sources are shown in Figure 15. The column density and the excitation temperature are derived by utilizing the least-squares fitting. The column density is derived from the interception of a diagram, and its slope gives us the excitation temperature.

In addition, the column density of the molecular hydrogen is estimated from the continuum emission from the dust with the same way as Hernandez-Hernandez et al. (2014), where the gas mass is calculated as

$$M_{\text{gas}} = \frac{S_{\nu} D^2 R_{\text{d}}}{B_{\nu}(T_{\text{d}}) \kappa_{\nu}}. \quad (2)$$

where S_ν , D , R_d , κ_ν , and $B_\nu(T_d)$ are the flux density, distance to the core, gas-to-dust ratio, the dust opacity per unit dust mass, and the Planck function at the dust temperature (T_d), respectively. As described in [Hernández-Hernández et al. \(2014\)](#), by assuming R_d of 100, and κ_ν of $0.74 \text{ cm}^2 \text{ g}^{-1}$, and using the Rayleigh-Jeans approximation, the equation to obtain the hydrogen column density at 1.3 mm is obtained as follow:

$$\left[\frac{N_{\text{H}_2}}{\text{cm}^2} \right] = \frac{2.35 \times 10^{16}}{\theta^2} \left[\frac{S_\nu}{\text{Jy}} \right] \left[\frac{T_d}{\text{K}} \right]^{-1}, \quad (3)$$

where θ is the source size in radians. In our work, we use the angular resolution of our observations as θ . S_ν is obtained by the procedure that we employ to subtract the continuum emission. We use the spectral window whose center frequency is 205.849 in Set 1, since the largest number of channels in this window would be useful to obtain the dust continuum level. We approximately use the excitation temperature of CH₃OH as T_d .

3.3. Abundances

The obtained column densities and the excitation temperatures of H₂, CH₃OH, CH₃NH₂, and CH₂NH are summarized in Table 15. CH₃NH₂ column densities are high in NGC6334I MM1 and G10.47+0.03, with their column densities of 1.0×10^{18} and $9.4 \times 10^{17} \text{ cm}^{-2}$, respectively. In addition, CH₃OH column density of $1.3 \times 10^{18} \text{ cm}^{-2}$ in G10.47+0.03 is the highest in our sources. The high abundance of N-bearing species in NGC6334I is contrary to our previous study in [Suzuki et al. \(2018\)](#), where we found that N-bearing species is rich in G10.47+0.03 while they are poor in NGC6334I region. Since the spatial distribution of CH₃OH is much extended than those of CH₂NH and CH₃NH₂ in NGC 6334I region, it is possible that the abundances of N-bearing species are underestimated than O-bearing species in [Suzuki et al. \(2018\)](#) due to the difference of source size. The obtained excitation temperature of G10.47+0.03 is 1466 K, which is much higher than the report of [Ohishi et al. \(2019\)](#), where the excitation temperature of G10.47+0.03 was less than 45 K. Probably the single dish observation by [Ohishi et al. \(2019\)](#) detected extended structure surrounding this core, which is resolved out with our interferometric observation.

Since we could not detect CH₃NH₂ transition toward NGC6334I MM3 region, the upper limit of CH₃NH₂ column density is obtained by assuming the excitation temperature of 170 K, corresponding to that of CH₃OH. With this excitation temperature, 16, 2, B2 \rightarrow 16, 1, B1 transition gives us the upper limit of the column density. With the r.m.s level of 0.5 K for this transition and line width of 6.0 km s^{-1} , we get the upper limit of column density of $1.0 \times 10^{16} \text{ cm}^{-2}$ with 3 sigma noise level. In addition, CH₂NH abundances are not determined from the rotation diagram method toward NGC6334I MM1 and MM3 due to the limited range of detected transitions. Therefore the excitation temperatures are fixed to be 120 and 170 K, respectively, for MM1 and MM3 to derive the column densities. Then the range of CH₂NH column densities for MM1 and MM3 are, respectively, from 0.3 to 1.3×10^{17} and from 0.4 to $1.5 \times 10^{15} \text{ cm}^{-2}$. Three cores in NGC6334I regions, MM1, MM2, and MM3, are the chemically interesting regions. As it has been reported by [Bøgelund et al. \(2019\)](#), the abundances of CH₃NH₂ and CH₂NH differ by orders of magnitude in NGC6334I MM1, MM2, and MM3. Our estimated column densities of CH₂NH and CH₃NH₂ agree well with [Bøgelund et al. \(2019\)](#) except for CH₃NH₂ in NGC6334I MM1, where our obtained abundance is higher than their work by about a factor of three. Since our observed position in NGC6334I is offsetted by about $2''$ compared to [Bøgelund et al. \(2019\)](#), this difference would not be surprising. In addition, our receiver set enables us to obtain the column density of CH₃OH toward MM1, MM2, and MM3 simultaneously. The similar column densities of CH₃OH in NGC6334I MM1, MM2, and MM3 clearly show the depletion of only N bearing species toward MM2 and MM3.

For G31.41+0.03, W51 e2, and W51 e8, we report the abundance of CH₃NH₂ for the first time. Their excitation temperatures and column densities are 79 K and $3.2 \times 10^{17} \text{ cm}^{-2}$ for G31.41+0.03, 95 K and $1.9 \times 10^{17} \text{ cm}^{-2}$ for W51 e2, and 131 K and $2.5 \times 10^{17} \text{ cm}^{-2}$ for W51 e8. The observed abundance ratios of “CH₃NH₂/CH₂NH” and “CH₃NH₂/CH₃OH” are shown in Table 16.

4. COMPARISON WITH CHEMICAL MODELING

In this section, we evaluate our observational results using our chemical model ([Suzuki et al. 2018](#)). Since the formation process of CH₃OH is well known to be via the grain surface hydrogenation processes to CO, the molecular ratio of “CH₃NH₂/CH₃OH” is the essential to test if CH₃NH₂ is formed via the successive hydrogenation processes to HCN.

We use the chemical model described in Suzuki et al. (2018) for this comparison. In this work, we used the gas-phase chemical network `kida.uva.2014`² (Wakelam et al. 2015), and the grain surface reactions in Garrod (2013). With these reaction sets, we updated the formation process of CH_3NH_2 . We added the hydrogenation processes of HCN on the grain surface ($\text{HCN} + 2\text{H} \rightarrow \text{H}_2\text{CN}$, and $\text{H}_2\text{CN} + 2\text{H} \rightarrow \text{CH}_3\text{NH}_2$) as described in Suzuki et al. (2016), resulting in the increase of CH_3NH_2 abundance. In total, 489 species composed of 13 elements (H, He, C, N, O, Si, S, Fe, Na, Mg, Cl, P, F) were included. To simulate the physical conditions in hot cores, we used the two stage physical model, where the free-fall collapse is followed by a dynamically-static warm up by following Garrod (2013). In our standard model, the cold collapse phase started from $n_{\text{H}_2} = 3 \times 10^3 \text{ cm}^{-3}$ to final post collapse density of $n_{\text{H}_2} = 2 \times 10^7 \text{ cm}^{-3}$. The increase in visual extinction during collapse leads to the minimum dust-grain temperature of 8 K followed by a warm-up from 8 to 400 K; during this phase, the gas and dust temperatures are assumed to be well coupled and the gas density is fixed. We employed the fast warm-up models described in Garrod (2013), whose timescale for the warm-up phases is 7.12×10^4 years, but continue calculation fixing the temperature. Since the weak hydrogen recombination lines of our sources suggest the young ages of the cores, we stopped the simulations at 1.0×10^6 years. The gravitational constant B is the parameter to slow down the collapse assuming the turbulence or the magnetic field (Nejad et al. 1990). The standard model used B to be unity, which is the case of free fall. The values of the gravitational constant B , the peak temperature, the peak density, and the timescale of warm-up phase are free parameters.

We show our simulation results in Figure 16 with our standard model. The simulated fractional abundances of CH_3OH , CH_3NH_2 , and CH_2NH , compared to the total proton density in the gas phase and on grains (sum of molecular abundances in the grain mantle and on the grain surface) are shown by dotted and solid lines, respectively. The time of zero year is corresponding to the beginning of the warm-up phase. As we discussed in the previous studies, CH_2NH is expected to be efficiently formed in the gas phase reaction of “ $\text{CH}_3 + \text{NH} \rightarrow \text{CH}_2\text{NH} + \text{H}$ ”, while CH_3NH_2 is built on grain surface via successive hydrogenation processes to HCN (Suzuki et al. 2016, 2018), similar to CH_3OH . When the grain surface temperature gets high enough, these species sublime from grains, leading to the sudden increase of the gas phase molecular abundance. The sublimation of CH_3NH_2 happens at $\sim 6.2 \times 10^4$ years, when the dust temperature is ~ 130 K, while the sublimation of CH_3OH happens when the dust temperature is ~ 110 K due to the smaller binding energy. Since CH_3NH_2 is frozen before 6.2×10^4 years, the gas phase abundance ratio before this age is not meaningful. We compare the fractional abundances of CH_3OH , CH_3NH_2 , and CH_2NH with our observation. Considering the errors and assumptions both in the simulations and the observations, we set a criteria to be factor of 10 to see if our model roughly reproduce the observed fractional abundances. The observed fractional abundances of CH_3OH , CH_3NH_2 , and CH_2NH compared to the number of atomic hydrogen are, respectively, ranging from 3.6×10^{-9} - 8.5×10^{-8} , 5.0×10^{-9} - 3.8×10^{-8} , and 1.3×10^{-10} - 2.3×10^{-9} . Hence our criteria to constrain the simulated fractional abundances of CH_3OH , CH_3NH_2 , and CH_2NH are, respectively, 3.6×10^{-10} - 8.5×10^{-7} , 5.0×10^{-10} - 3.8×10^{-7} , and 1.3×10^{-11} - 2.3×10^{-8} . In Figure 16, the simulated fractional abundances of CH_3NH_2 and CH_2OH agree with the observation at the later phase of the simulation. However, the fractional abundance of CH_2NH is always higher than the observed value. As discussed in Suzuki et al. (2016), the formation rate of CH_2NH from radicals are well investigated (see also KIDA database) and therefore this overproduction would not be due to the wrong formation rate. We confirmed this overproduction of CH_2NH under the different gas temperatures of 200 and 300 K, and hence the temperature would not be a key to solve this discrepancy. Other possibility would be the lack of the destruction processes of CH_2NH in the model, or the overproduction of NH and CH_3 radicals, which are the precursors of CH_2NH , by the cosmic rays or the secondary UV photons in the gas phase.

The molecular ratios of “ $\text{CH}_3\text{NH}_2/\text{CH}_3\text{OH}$ ” after the sublimation of CH_3NH_2 are presented in Figure 16. Both CH_3OH and CH_3NH_2 are formed on grains during the warm-up phase and destroyed simultaneously in the gas phase after the sublimation by reactive radicals, ions, and cosmic rays, and hence the range of “ $\text{CH}_3\text{NH}_2/\text{CH}_3\text{OH}$ ” is very limited. The ratio of “ $\text{CH}_3\text{NH}_2/\text{CH}_3\text{OH}$ ” is 0.1 at first, and it increases slightly to 0.4 at the end of the simulation, since CH_3OH is efficiently destroyed by C and H_3O^+ , while the destruction of CH_3NH_2 by these species are not included in `kida.uva.2014`. Therefore the slight increase of “ $\text{CH}_3\text{NH}_2/\text{CH}_3\text{OH}$ ” may be due to the lack of destruction processes of CH_3NH_2 . The ratio of “ $\text{CH}_3\text{NH}_2/\text{CH}_3\text{OH}$ ” is the ideal tool to discuss the CH_3NH_2 chemistry. First, the “ $\text{CH}_3\text{NH}_2/\text{CH}_3\text{OH}$ ” ratio is free from the uncertainty of the hydrogen column density. Second, the similarity in CH_3NH_2 and CH_3OH chemistry can reduce the uncertainty of the physical parameters, enabling us to focus on the formation process of CH_3NH_2 .

² <http://kida.obs.u-bordeaux1.fr/>

To assume the different physical evolution of hot cores, we perform nine simulations under the different gravitational constant B, the temperature, the density, and the warm-up timescale. The physical parameters are basically same as the standard model but only one parameter is changed to develop other models. Here, the gravitational constant B is set to be 0.7, 0.2, and 0.1. The temperature is changed from 400 to 200 K. The gas density is put to be 1×10^6 and $1 \times 10^8 \text{ cm}^{-3}$. The two different warm-up timescales, 7.12×10^3 and 7.12×10^5 years, are prepared and named as long and short warm-up time scale model. For the comparison with the observational result, we set the criteria that the fractional abundances of CH₃OH and CH₃NH₂ are, respectively, in the range of 3.6×10^{-10} - 8.5×10^{-7} and 5.0×10^{-10} - 3.8×10^{-7} . Then, we get the “CH₃NH₂/CH₃OH” ratio of between 0.09 and 0.39, except for the cases of different value of B, as is summarized in Table 16. It is interesting that only the constant B strongly changes the “CH₃NH₂/CH₃OH” ratio among our free parameters. The parameter B controls the timescale of collapsing phase, it leads to the different HCN and CO abundances on grains at the collapsing phase prior to the warm-up phase. With its low binding energy, the abundance of CO decreases by the gas phase chemistry if the timescale of the collapsing phase is long due to high value of B. Since CH₃OH is the products of hydrogenation processes to CO, it changes the abundance of CH₃OH and “CH₃NH₂/CH₃OH” ratio as well.

The abundance ratios reported by the model of Garrod (2013) are also summarized in this table to discuss the CH₃NH₂ chemistry. Though both of our model and the model of Garrod (2013) include the radical-radical reactions to form CH₃NH₂ (e.g., CH₃ + NH₂) on grain surface, only our model includes the hydrogenation process to HCN and therefore our model shows much higher abundance of CH₃NH₂. If we exclude the hydrogenation process to HCN on grains from our model, we get the close CH₃NH₂ abundance to Garrod (2013). Thus, the result of Garrod (2013) showed the “CH₃NH₂/CH₃OH” ratio of less than 0.007, which is almost 50 times smaller than our model with the same physical evolution. According to Table 16, the range of observed “CH₃NH₂/CH₃OH” ratio is between 0.11 and 2.2. These high values are not explained by the model of Garrod (2013). Since our simulations show the “CH₃NH₂/CH₃OH” ratio of more than 0.2 for all cases, they show good agreement with the observed ratios. These results clearly indicate the importance of hydrogenation process to form CH₃NH₂.

Our conclusion that CH₃NH₂ is built through the successive hydrogenation to HCN is different from previous study of Bøgelund et al. (2019). In Bøgelund et al. (2019), the authors observed NGC6334I and derived the CH₃NH₂ abundances to be 2.7×10^{17} , 6.2×10^{16} , and $3.0 \times 10^{15} \text{ cm}^{-2}$ for MM1, MM2, and MM3, respectively. With these ratios, they obtained the “CH₃NH₂/CH₃OH” ratio ranging from $\sim 5 \times 10^{-3}$ to $\sim 5 \times 10^{-4}$, which agrees with the peak abundance ratio by the fast warm-up model in Garrod (2013) within a factor of five. Therefore they suggested that CH₃NH₂ is built via recombination process of radical species (CH₃ + NH₂). Their low value of “CH₃NH₂/CH₃OH” ratio is contrary to our result. Especially there is a critical disagreement in “CH₃NH₂/CH₃OH” ratio toward NGC6334 region, although our CH₃NH₂ column density is not so different with their work. This disagreement comes from the CH₃OH column density to obtain “CH₃NH₂/CH₃OH” ratio.

We believe our “CH₃NH₂/CH₃OH” ratios are more reliable for few reasons. First, Bøgelund et al. (2019) observed only one transition of the isotope of CH₃OH, which would lead the uncertainty of the CH₃OH abundance. Second, if we apply their observation results and assume the CH₃NH₂ column density of $2.7 \times 10^{17} \text{ cm}^{-2}$ and “CH₃NH₂/CH₃OH” ratio of 1×10^{-3} , then the CH₃OH column density should be $2.7 \times 10^{20} \text{ cm}^{-2}$. This surprisingly high CH₃OH column density is not consistent with the previous studies. The column density of CH₃OH can be roughly estimated from the previous observation of single dish telescope by assuming the source size. Ikeda et al. (2001) found that the CH₃OH column density toward NGC6334I was $3.4 \times 10^{16} \text{ cm}^{-2}$ under the assumption of the source size of 20". Our mapping result suggests that the source size of CH₃OH is $\sim 5''$ in NGC6334I region. Then, from Ikeda et al. (2001), the CH₃OH column density can be estimated to be $3.4 \times 10^{16} \times (20''/5'')^2 = 5.4 \times 10^{17} \text{ cm}^{-2}$. Therefore the column density of CH₃OH used in Bøgelund et al. (2019) would be strongly overestimated. The column density of $5.4 \times 10^{17} \text{ cm}^{-2}$ rather agrees with our CH₃OH column densities toward NGC6334I region.

4.1. Comparison with Other Sources

The CH₃NH₂ and CH₃OH abundances were investigated toward Sgr B2 (M) and (N) by Belloche et al. (2013) and Neill et al. (2014). According to Belloche et al. (2013) and Neill et al. (2014), the ratio of “CH₃NH₂/CH₃OH” in Sgr B2 (N) are 0.03 and 0.1, respectively. The different ratios claimed by different authors would come from the smaller source size of CH₃NH₂, since the spatial resolution by Neill et al. (2014) is higher than Belloche et al. (2013). The “CH₃NH₂/CH₃OH” ratio of 0.1 is close to our values in NGC6334I MM2, G10.47+0.03, G31.41+0.3, and W51 e8.

The “CH₃NH₂/CH₃OH” ratio in NGC6334I MM1 and W51 e2 are higher than Sgr B2. On the other hand, the small value of “CH₃NH₂/CH₃OH” in Sgr B2(M) is close to NGC6334I MM3.

We also show the analysis of CH₃NH₂ abundance toward Orion KL Hot core using archival data of ALMA in the Appendix of this paper. The derived column density of CH₃NH₂ toward Orion KL is 1.6×10^{16} cm⁻². The CH₃OH column densities toward Orion KL-W region is found in Peng et al. (2012). Their CH₃OH contour map suggests that the CH₃OH abundance at the position of the Hot core would be close to the position of KL-W region. In this case, CH₃OH column density should be 9.2×10^{17} cm⁻². Therefore we get the “CH₃NH₂/CH₃OH” ratio of 0.017 for Orion KL Hot Core.

The small “CH₃NH₂/CH₃OH” ratio in Sgr B2 (M) and Orion KL Hot core is similar to NGC6334I. This small ratio is not explained by our chemical model under the possible range of the physical parameters. The disagreement may be due to the different physical evolution from the other sources.

Finally, we note that this survey was performed toward CH₂NH-rich sources reported in Suzuki et al. (2016). Therefore our source samples may be biased toward N-bearing species rich sources. Further expansion of CH₃NH₂ survey towards other hot cores would be useful to reveal more general picture of hot core chemistry. The survey observation of low-mass protostar is also an interesting topic. IRAS16293-2422 is the only hot corino where “CH₃NH₂/CH₃OH” ratio was investigated. The reported “CH₃NH₂/CH₃OH” ratio of less than 5.3×10^{-5} is extraordinary lower than our result. It would be worth to explore the chemical difference between the high-mass and the low-mass protostars by future surveys.

5. CONCLUSION

The main results of this paper are summarized as follows:

1. We performed a survey observation of CH₃NH₂, CH₂NH, and CH₃OH toward NGC6334I, G10.47+0.03, G31.41+0.3, and W51 e1/e2 region with ALMA. NGC6334I were resolved into MM1, 2, and 3, and W51 e1/e2 are resolved into e2 and e8. In total, we analyzed the molecular abundances at seven hot cores. CH₃NH₂, CH₂NH, and CH₃OH are detected for all sources except for NGC6334I MM3, where CH₃NH₂ was not detected.
2. The excitation temperature and column density of CH₃NH₂, CH₂NH, and CH₃OH were obtained by the rotation diagram method. The CH₃NH₂ abundances are obtained for G31.41+0.03, W51 e2, and W51 e8 for the first time. NGC6334I and G10.47+0.03 are especially CH₃NH₂-rich sources with their column densities of $\sim 10^{18}$ cm⁻². For other sources, the column densities of CH₃NH₂ are typically $\sim 10^{17}$ cm⁻², but less than 3×10^{15} cm⁻² for NGC6334I MM3.
3. The observed fractional abundances for CH₃OH, CH₃NH₂, and CH₂NH are, respectively, $\sim 10^{-8}$, $\sim 10^{-8}$, and $\sim 10^{-9}$. The observed fractional abundance of CH₂NH is not explained by our modeling within a factor of 10, while those of CH₃OH and CH₃NH₂ show the agreement. This discrepancy would be due to the lack of the destruction process of CH₂NH, or the overproduction of radicals to form CH₂NH.
4. We obtained the observed “CH₃NH₂/CH₃OH” ratio of between 0.11 and 2.2. This high “CH₃NH₂/CH₃OH” ratio is not explained by the recombination of radicals as suggested by Garrod (2013) and the grain surface hydrogenation process discussed in Suzuki et al. (2016) is required. Our conclusion is different from the previous observation toward NGC6334I region by Bøgelund et al. (2019), though the obtained CH₃NH₂ column density agrees well. The difference is due to the method to measure CH₃OH column density, and our work would be more accurate than Bøgelund et al. (2019).
5. NGC6334I MM3 shows extremely low “CH₃NH₂/CH₂NH” ratio of <0.02, which is close to Orion KL Hot core and Sgr B2 (M). Such small molecular ratio is not explained by our current chemical model by changing the physical parameters. The detailed discussion of these sources are remained to the future works. In addition, it is possible that our source selection is biased to N-bearing molecule rich sources by selecting the target from our previous CH₂NH survey. The extension of this survey toward various sources would be important to further expand our knowledge.

This paper makes use of the following ALMA data: ADS/JAO ALMA#2017.1.01248.S. ALMA is a partnership of ESO (representing its member states), NSF (USA) and NINS (Japan), together with NRC (Canada), MOST and

ASIAA (Taiwan), and KASI (Republic of Korea), in cooperation with the Republic of Chile. The Joint ALMA Observatory is operated by ESO, AUI/NRAO and NAOJ. The National Radio Astronomy Observatory is a facility of the National Science Foundation operated under cooperative agreement by Associated Universities, Inc. This study was supported by the Astrobiology Program of National Institutes of Natural Sciences (NINS) and by the JSPS Kakenhi Grant Numbers 19K03936, 19H05069, and 19K14753.

APPENDIX

The Orion-KL is the nearest massive star-forming region, which is located approximately 418 ± 6 pc away from the sun (Kim et al. 2008). Its proximity and rich molecular composition make this region well suited for astrochemical study. Since this region was discovered in 1967 (Kleinmann et al. 1967), numerous studies including line survey have been conducted so far (e.g., Pagani et al. 2017; Feng et al. 2015; Gong et al. 2015; Turner 1991).

In Orion-KL, several remarkable sources called Hot core and Compact ridge are known as regions where many organic molecules exist (Blake et al. 1987). Hot core is known as a high-density (10^6 cm^{-3}) region with a warm (~ 150 K), compact (< 0.05 pc) clump (Zapata et al. 2011), and Compact ridge is also known to be a warm and dense region. Many previous studies have revealed that the chemical composition is different between these regions. While many molecules containing nitrogen (e.g., NH₃, CH₃CN, etc.) are observed in Hot core, O-bearing species (e.g., CH₃OH, CH₃OCH₃, etc.) are observed in Compact ridge (Favre et al. 2011).

The abundance of CH₃NH₂ is analyzed using archive data of Orion KL Hot core (ADS/JAO ALMA#2013.1.00553.S. and 2011.0.00009.SV). The description of this observation is found in Pagani et al. (2017). We used CASA software V.5.0.0 during the procedure to analyze observational data. Cycle 2 data cube was already calibrated by Pagani et al. (2017), and the reduced data are available on the web site of CDS (Centre de Données astronomiques de Strasbourg)³. The continuum emission in SV data was subtracted using the line free channels in the (u, v) domain by CASA task UVCNTSUB with channels. After that, CASA task TCLEAN was used to deconvolve the images by applying natural weighting.

Figure 6 shows the integrated intensity maps of the 6 transitions in Table 14, created by the CASA task IMMOMENT. CH₃NH₂ emission appears mainly at Hot core and partially at IRc7. According to previous work (e.g., Feng et al. 2015; Gong et al. 2015), N-bearing species tend to have the similar peak at or near Hot core. The distribution of CH₃NH₂ also shows the same trend.

The spectrum were extracted from the region of $1''.0$ in diameter around Hot core ($RA_{J2000} : 05^{\text{h}}35^{\text{m}}14^{\text{s}}.580$, $Dec_{J2000} : -05^{\circ}22'31''.029$). The Gaussian fitting was performed to obtain FWHM line widths Δv and the mean local standard of rest velocity V_{LSR} of the emission lines. Table 14 shows the all the detected CH₃NH₂ transitions with their line parameters. A transition at 242.262 GHz is reported for the first time in this work, while other lines are already detected in Pagani et al. (2017) The average LSR velocity and FWHM line width are estimated to be 4.84 km s^{-1} and 4.16 km s^{-1} , respectively. V_{LSR} are consistent with those reported by Feng et al. (2015) for N-bearing COMs observed toward Hot core (e.g, 4.9 km s^{-1} for CH₂CHCN, 5.1 km s^{-1} for CH₃CH₂CN). On the other hand, the line width of CH₃NH₂ is narrower than those of other molecules in Hot core (typically $5\text{--}15 \text{ km s}^{-1}$, Pagani et al. 2017). With the rotation diagram method, the column density and the excitation temperature of CH₃NH₂ is obtained to be $1.6 \pm 0.6 \times 10^{16} \text{ cm}^{-2}$ and 77 ± 17 K. Since Pagani et al. (2017) obtained the CH₃NH₂ column density of $1 \times 10^{16} \text{ cm}^{-2}$ through LTE fitting on spectra, our result agrees well with their result.

REFERENCES

- Altwegg, K., Balsiger, H., Bar-Nun, A., et al. 2016, *Sci*, 2, id=e1600285
- Bøgelund, E. G., McGuire, B. A., Hogerheijde, M. R., et al 2019, ArXiv e-prints[arXiv:1902.07060]
- Blake, G. A., Sutton, E. C., Masson, C. R., & Phillips, T. G. 1987, *ApJ*, 315, 621
- Blagojevic, V., Petrie, S., & Bohme, D. K. 2003, *MNRAS*, 339, L7
- Brogan, C. L., Hunter, T. R., Cyganowski, C. L., et al., 2016, *ApJ*, 832, 187
- Belloche, A., Müller, H. S. P., Menten, K. M., Schilke, P., & Comito, C. 2013, *A&A*, 559, A47
- Belloche, A., Garrod, R. T., Müller, H. S. P., & Menten, K. M. 2014, *Sci*, 345, 1584

³ <http://cdsarc.u-strasbg.fr/viz-bin/qcat?J/A+A/604/A32>

- Churchwell, E., Walmsley, C. M., & Cesaroni, R., 1990, A&AS, 83, 119
- Cesaroni, R., Churchwell, E., Hofner, P., Walmsley, C. M., & Kurtz, S 1994, A&A, 288, 903
- Cesaroni, R., Hofner, P., Walmsley, C. M., & Churchwell, E. 1998, A&A, 331, 709
- Cesaroni R., Hofner P., Araya E., Kurtz S., 2010, A&A, 509, A50
- Dickens, J. E., Irvine, W. M., Devries, C. H., & Ohishi, M. 1997, ApJ, 479, 312
- Favre, C., Despois, D., et al. 2011, A&A, 532, A32
- Feng, S., Beuther, H., Henning, T., Semenov, D., Palau, A., & Mills, E. A. C. 2015, A&A, 581, A7
- Fourikis, N., Takagi, K., & Morimoto, M. 1974, ApJ, 191, L139
- Garrod, R. T., 2013, ApJ, 765, 60
- Gaume, R. A., Johnston, K. J., & Wilson, T. L. 1993, ApJ, 417, 645
- Goddi, C., Ginsburg, A., & Zhang, Q 2016, A&A, 589, A44
- Godfrey, P. D., Brown, R. D., Robinson, B. J., & Sinclair, M. W. 1973, Astrophys. Lett., 13, 119
- Gong, Y., et al. 2015, A&A, 581, A48
- Halfen, D. T., Iyushin, V. V., & Ziurys, L. M. 2013, ApJ, 767, 66
- Hernández-Hernández, V., Zapata, L., Kurtz, S., & Garay, G., 2014, ApJ, 786, 38
- Hirota, T., Kim, M. K., Kurono, Y., & Honma, M. 2015, ApJ, 801, 82
- Hollis, J. M., Jewell P. R., Lovas, F. J., Remijan, A, & Møllendal, H 2004, ApJ, 610, L21
- Hollis, J. M., Jewell, P. R., Lovas, F. J., & Remijan, A., ApJ, 613, L45
- Holtom, P. D., Bennett, C. J., Osamura, Y., Mason, N. J., & Kaiser, R. I. 2005, ApJ, 626, 940
- Hunter, T. R., Brogan, C. L., Megeath, S. T., et al 2006, ApJ, 649, 888
- Ikeda, M., Ohishi, M., Nummelin, A., et al. 2001, ApJ, 560, 792
- Ilyushin, V. V., & Lovas, F. J. 2007, JPCRD, 36, 1141
- Jones, P. A., Burton, M. G., Cunningham, M. R., et al. 2008, MNRAS, 386, 117
- Jones, P. A., Burton, M. G., Tothill, N. F. H., & Cunningham, M. R. 2011, MNRAS, 411, 2293
- Kaifu, N., Morimoto, M., Nagane, K., et al. 1974, ApJ, 191, L135
- Kim, Y. S. & Kaiser, R. I. 2011, ApJ, 729, 68
- Kim, M. K., et al. 2008, PASJ, 60, 991
- Kleinmann, D. E., & Low, F. J. 1967, ApJS, 149, L1
- Lee, C-W., Kim, J-K., Moon, E-S., Minh, Y-C., & Kang, H. 2009, ApJ, 697, 428
- Ligterink, N. F. W., Tenenbaum, E. D., & van Dishoeck, E. F., A&A, 576, A35
- Ligterink, N. F. W., Calcutt, H., Coutens, A., et al, 2018, A&A, 619, A28
- McGuire, B. A., Carroll, P. B., Loomis, R. A., et al 2016, Sci, 352, 1449
- Menten, K. M., Reid, M. J., Forbrich, J., & Brunthaler, A. 2007, A&A, 474, 515
- Nejad, L. A. M., Williams, D. A., & Charnley, S. B. 1990, MNRAS, 246, 183
- Neill, J. L., Bergin, E. A., Lis, D. C., et al. 2014, ApJ, 789, 8
- Nummelin, A., Bergman, P., Hjalmarsen, A., et al. 1998, ApJS, 117, 427
- Ohishi, M., Suzuki, T., Hirota, T., Saito, M., & Kaifu, N. 2019, PASJ, in print
- Pegani, L., Favre, C., Goldsmith, P. F., et al 2017, A&A, 604, A32
- Peng, T.-C., Despois, D., Brouillet, N., Parise, B., & Baudry, A. 2012 A&A, 543, A152
- Pizzarello, S., Feng, X., Epstein, S., & Cronin, J. R. 1994, GeCoA, 58, 5579
- Qin, S.-L., Wu, Y., Huang, M., et al. 2010, ApJ, 711, 399
- Reid M. J., Menten K. M., Brunthaler A., et al., ApJ, 783, 130 (2014)
- Rolfs, R., Schilke, P., Zhang, Q., & Zapata, L. 2011, A&A, 536, A33.
- Sanchez-Monge, A., Schilke, P., Ginsburg, A., Cesaroni, R., & Schmiedeke, A. 2018, A&A 609, A101
- Shi, H., Zhao, J-H., & Han, J, L. 2010, ApJ, 710, 843
- Singh, A., Misra, S, A., & Tandon, P. 2013, Astron, 13, 8, 912
- Suzuki, T., Ohishi, M, Hirota, T., et al. 2016, ApJ, 825, 79
- Suzuki, T., Majumdar, L., Ohishi, M., et al. 2018 ApJ, 863, 51
- Sutton, E. C., Jaminet, P. A., Danchi, W. C., & Blake, G. A. 1991, ApJS77, 255
- Tang, Y-W., Ho, P. T. P., Koch, P. M., et al., 2009, ApJ, 700, 251
- Theule, P., Borget, F., Mispelaer, F., et al. 2011, A&A, 534, A64
- Turner, B. E. 1989, ApJS, 70, 539
- Turner, B. E, 1991 ApJS, 76, 617
- Turner, B. E., Terzieva, R., & Herbst, E. 1999, ApJ, 518, 699
- Wakelam V., et al., ApJS, 217, 20 (2015)
- Walsh, A. J., Thorwirth, S., Beuther, H., & Burton, M. G. 2010, MNRAS, 404, 1396
- Widicus Weaver, S. L., Laas, J C., Zuo, Luyao et al., 2017, ApJS, 232, 3

- Wood, D. O. S., & Churchwell, E. 1989, ApJ, 69, 831
- Woon, D. E. 2002, ApJ, 571, L177
- White, G. J., Araki, M., Greaves, J. S., Ohishi, M., & Higginbottom, N. S. 2003, A&A, 407, 589
- Zapata, L. A., Loinard, L., Schmid-Burgk, J., et al. 2011, ApJ, 726, L12
- Zernickel, A., Schilke, P., Schmiedeke, A., et al. 2012, A&A, 546, A87
- Zhang, Q., & Ho, P. T. P., 1997, ApJ, 488, 214

Table 1. List of Observed Sources

Source	RA _{J2000} h m s	Dec _{J2000} ° ' "	V _{LSR} (km s ⁻¹)	distance (kpc)	X[CH ₂ NH] (x10 ⁻⁸)	reference
NGC6334I	17 20 53.4	-35 47 1.0	-7	1.3	0.24	1, 3
G10.47+0.03	18 08 38.13	-19 51 49.4	67	8.5	3.1	1, 3
G31.41+0.3	18 47 34.6	-01 12 43.0	97	7.9	0.88	1, 4
W51 e1/e2	19 23 43.77	+14 30 25.9	57	5.4	0.28	1, 3

NOTE— The coordinate of the phase center, radial velocity, and the distance to sources are summarized. The fractional abundance of CH₂NH compared to hydrogen reported in Suzuki et al. (2016) is also shown. References. (1) Ikeda et al. (2001) (2) Menten et al. (2007) (3) Reid et al. (2014) (4) Churchwell et al. (1990)

Table 2. Observation Parameters

	NGC6334I Set1	NGC6334I Set2	G10.47+0.03 Set1	G10.47+0.03 Set2
Observation date	2018 May 13	2018 May 14	2018 May 13	2018 May 14
Configuration	C43-2	C43-1	C43-2	C43-1
Phase Center (° ' ")	07:20:53.4, -35:47:1.0	07:20:53.4, -35:47:1.0	08:08:38.1, -19:51:49.4	08:08:38.1, -19:51:49.4
Band	Band 5	Band 6	Band 5	Band 6
Time on Source (minutes)	21	6	40	11
Number of antennas	43	46	43	43
Spectral Resolution (MHz)	487.5	487.5	487.5	487.5
Maximum Recoverable Scale (")	11.8	8.8	11.8	8.8
Bandpass Calibrator	J1617-5848	J1924-2914	J1924-2914	J1924-2914
Phase Calibrator	J1733-3722	J1733-3722	J1832-2039	J1832-2039
Flux Calibrator	J1617-5848	J1924-2914	J1924-2914	J1924-2914
Angular Resolution (" × ")	1.50 × 1.18	1.04 × 1.56	1.38 × 1.25	1.20 × 0.94

NOTE—

Table 3. Observation Parameters (continued)

	G31.41+0.3 Set1	G31.41+0.3 Set2	W51 e1/e2 Set1	W51 e1/e2 Set2
Observation date	2018 May 13	2018 May 15	2018 May 13	2018 May 14
Configuration	C43-2	C43-2	C43-2	C43-2
Phase Center	18:47:34.6, -01:12:43.0	18:47:34.6, -01:12:43.0	19:23:43.8, 14:30:25.9	19:23:43.8, 14:30:25.9
Band	Band 5	Band 6	Band 5	Band 6
Time on Source (minutes)	42	12	33	13
Number of antennas	43	46	43	46
Spectral Resolution (MHz)	487.5	487.5	487.5	487.5
Maximum Recoverable Scale (")	11.6	8.8	11.8	8.8
Bandpass Calibrator	J2000-1748	J2000-1748	J2000-1748	J1751+0939
Phase Calibrator	J1851+0035	J1851+0035	J1922+1530	J1922+1530
Flux Calibrator	J2000-1748	J1751+0939	J2000-1748	J1751+0939
Angular Resolution (" × ")	1.25 × 0.79	1.13 × 0.98	1.32 × 1.19	1.15 × 1.05

NOTE—

Table 4. Observed Frequency Range

Set 1			Set 2		
Center Frequency (rest, GHz)	Band Width (GHz)	Number of Channels	Center Frequency (rest, GHz)	Band Width (GHz)	Number of Channels
192.212	0.234	480	247.611	0.234	480
191.959	0.234	480	247.967	0.234	480
191.732	0.234	480	248.838	0.234	480
191.462	0.234	480	249.192	0.234	480
193.795	0.234	480	249.443	0.234	480
193.415	0.234	480	250.161	0.234	480
192.622	0.234	480	250.219	0.234	480
192.469	0.234	480	250.507	0.234	480
203.050	0.938	1920	261.024	0.234	480
205.849	0.938	1920	261.219	0.234	480
			261.562	0.234	480
			261.805	0.234	480
			263.986	0.234	480
			264.172	0.234	480
			264.457	0.234	480
			264.752	0.234	480

NOTE—

Table 5. The Observed Transitions

Species	Frequency (MHz)	transition	transition	transition	→	transition	transition	transition	E _u (K)	Sμ ² (D ²)
		<i>J'</i>	<i>K'_a</i>	<i>Γ'</i>	→	<i>J''</i>	<i>K''_a</i>	<i>Γ''</i>		
CH ₃ OH	191732.99	6	3	<i>E</i>	→	7	2	<i>E</i>	96.5	1.4
	191810.50	4	1	<i>A</i> ⁺	→	3	1	<i>A</i> ⁺	37.6	3.0
	193415.33	4	0	<i>E</i>	→	3	0	<i>E</i>	36.3	3.2
	193441.61	4	-1	<i>E</i>	→	3	-1	<i>E</i>	28.8	3.0
	193454.37	4	0	<i>A</i> ⁺	→	3	0	<i>A</i> ⁺	23.2	3.2
	193471.43	4	3	<i>A</i> ⁺	→	3	3	<i>A</i> ⁺	73.0	1.4
	193471.54	4	3	<i>A</i> ⁻	→	3	3	<i>A</i> ⁻	73.0	1.4
	193474.42	4	3	<i>E</i>	→	3	3	<i>E</i>	70.9	1.4
	193488.05	4	2	<i>A</i> ⁻	→	3	2	<i>A</i> ⁻	60.9	2.4
	193488.96	4	-3	<i>E</i>	→	3	-3	<i>E</i>	85.9	1.4
	193506.57	4	1	<i>E</i>	→	3	1	<i>E</i>	44.3	3.1
	193510.75	4	2	<i>A</i> ⁺	→	3	2	<i>A</i> ⁺	60.9	2.4
	193511.23	4	-2	<i>E</i>	→	3	-2	<i>E</i>	49.1	2.4
	193511.34	4	2	<i>E</i>	→	3	2	<i>E</i>	45.5	2.4
	205791.23	1	1	<i>A</i> ⁺	→	2	0	<i>A</i> ⁺	16.8	1.0
	247611.04	18	3	<i>A</i> ⁻	→	18	2	<i>A</i> ⁺	446.6	17.4
	247967.93	23	1	<i>E</i>	→	23	0	<i>E</i>	661.4	11.7
	248885.48	16	3	<i>A</i> ⁻	→	16	2	<i>A</i> ⁺	365.4	15.3
	249192.86	16	-3	<i>E</i>	→	15	-4	<i>E</i>	378.3	4.7
	249419.90	15	3	<i>A</i> ⁻	→	15	2	<i>A</i> ⁺	328.3	14.3
249443.34	7	4	<i>A</i> ⁻	→	8	3	<i>A</i> ⁻	145.3	1.2	
249451.89	7	4	<i>A</i> ⁺	→	8	3	<i>A</i> ⁺	145.3	1.2	
250291.13	13	3	<i>A</i> ⁻	→	13	2	<i>A</i> ⁺	261.0	12.3	
250507.02	11	0	<i>A</i> ⁺	→	10	1	<i>A</i> ⁺	153.1	10.6	
261805.74	2	1	<i>E</i>	→	1	0	<i>E</i>	28.0	1.3	
CH ₂ NH		<i>J'</i>	<i>K'_a</i>	<i>K'_b</i>	→	<i>J''</i>	<i>K''_a</i>	<i>K''_b</i>		
	191462.82	3	0	3	→	2	0	2	18.4	5.3
	191959.30	3	2	2	→	2	2	1	49.9	2.9
	192212.32	4	1	3	→	4	0	4	39.8	9.8
	192469.59	3	2	1	→	2	2	0	50.0	2.9
	250161.68	7	1	6	→	7	0	7	97.2	13.8
263986.06	3	2	1	→	4	1	4	50.0	0.8	
CH ₃ NH ₂		<i>J'</i>	<i>K'_a</i>	<i>Γ'</i>	→	<i>J''</i>	<i>K''_a</i>	<i>Γ''</i>		
	192622.39	14	2	<i>E</i> ₁₋₁	→	14	1	<i>E</i> ₁₊₁	239.0	11.9
	193795.82	16	2	<i>B</i> ₂	→	16	1	<i>B</i> ₁	305.3	15.6
	202791.86	3	1	<i>E</i> ₂₋₁	→	2	0	<i>E</i> ₂₊₁	16.7	0.9
	203050.98	12	2	<i>E</i> ₁₋₁	→	12	1	<i>E</i> ₁₊₁	181.6	8.6
	203096.32	16	2	<i>E</i> ₁₊₁	→	16	1	<i>E</i> ₁₊₁	305.9	0.6
	248838.50	3	2	<i>B</i> ₁	→	3	1	<i>B</i> ₂	28.9	2.3
	249527.26	10	5	<i>E</i> ₂₊₁	→	11	4	<i>E</i> ₂₊₁	214.8	1.5
	250110.22	4	2	<i>A</i> ₁	→	4	1	<i>A</i> ₂	37.4	3.1
	250159.40	2	2	<i>B</i> ₂	→	2	1	<i>B</i> ₁	22.6	1.3
	250255.53	5	2	<i>E</i> ₁₊₁	→	5	1	<i>E</i> ₁₋₁	47.9	1.3
	250398.51	12	1	<i>E</i> ₁₋₁	→	11	2	<i>E</i> ₁₊₁	168.6	0.7
	260963.40	11	1	<i>B</i> ₂	→	10	2	<i>B</i> ₁	145.9	3.9
	261024.31	4	1	<i>E</i> ₂₊₁	→	3	0	<i>E</i> ₂₊₁	25.9	3.1
	261219.28	4	1	<i>B</i> ₁	→	3	0	<i>B</i> ₂	25.6	3.9
	261252.83	6	2	<i>B</i> ₁	→	6	1	<i>B</i> ₂	60.9	4.5
	261562.18	8	0	<i>B</i> ₁	→	7	1	<i>B</i> ₂	76.8	4.9
264172.18	4	1	<i>E</i> ₁₊₁	→	3	0	<i>E</i> ₁₊₁	25.9	3.7	
264457.13	9	2	<i>E</i> ₁₊₁	→	9	1	<i>E</i> ₁₋₁	111.8	3.4	
264752.35	7	2	<i>B</i> ₂	→	7	1	<i>B</i> ₁	75.8	5.1	

NOTE— The observed transitions of CH₃NH₂, CH₂NH, and CH₃OH are shown. E_u represents the energy of the upper state level, while Sμ² shows the product of the intrinsic line strength and the square of the permanent dipole moment.

Table 6. Detected Sources

Source	α (J2000)	δ (J2000)
	h m s	° ' "
NGC6334I MM1	17 20 53.433	-35 46 58.0
NGC6334I MM2	17 20 53.170	-35 46 58.6
NGC6334I MM3	17 20 53.416	-35 47 02.8
G10.47+0.03	18 08 38.258	-19 51 50.2
G31.41+0.3	18 47 34.320	-01 12 46.0
W51 e2	19 23 43.986	+14 30 34.6
W51 e8	19 23 43.890	+14 30 28.2
Orion KL Hot core	05 35 14.580	-05 22 31.029

NOTE— The coordinate, radial velocity, and the distance to sources are summarized. The fractional abundance of CH₂NH compared to hydrogen reported in Suzuki et al. (2016) is also shown. References. (1) Ikeda et al. (2001) (2) Menten et al. (2007) (3) Reid et al. (2014) (4) Churchwell et al. (1990)

Table 7. Observed Lines towards NGC6334I MM1

Species	→						Rest. freq (MHz)	Obs freq (MHz)	T _{MB} (K)	Δv (km s ⁻¹)	V _{LSR} (km s ⁻¹)	rms (K)	
	<i>J'</i>	<i>K'_a</i>	<i>Γ'</i>	→	<i>J''</i>	<i>K''_a</i>	<i>Γ''</i>						
CH ₃ OH	6	3	<i>E</i>	→	7	2	<i>E</i>	191732.99	191732.55	80.0	7.7	-6.3	1.32
	4	1	<i>A</i> ⁺	→	3	1	<i>A</i> ⁺	191810.50	191810.23	67.9	8.2	-6.6	2.23
	4	0	<i>E</i>	→	3	0	<i>E</i>	193415.33	193414.74	73.6	8.9	-6.1	2.63
	4	-1	<i>E</i>	→	3	-1	<i>E</i>	193441.61	193440.61	73.9	8.6	-5.5	2.43
	4	0	<i>A</i> ⁺	→	3	0	<i>A</i> ⁺	193454.37	193453.49	65.9	10.8	-5.6	0.81
	4	1	<i>E</i>	→	3	1	<i>E</i>	193506.57	193504.87	82.0	5.2	-4.4	1.93
	1	1	<i>A</i> ⁺	→	2	0	<i>A</i> ⁺	205791.23	205790.68	79.0	7.7	-6.2	4.86
	18	3	<i>A</i> ⁻	→	18	2	<i>A</i> ⁺	247611.04	247608.40	46.0	4.3	-3.8	1.86
	23	1	<i>E</i>	→	23	0	<i>E</i>	247967.93	247966.57	63.8	6.0	-5.4	2.71
	16	3	<i>A</i> ⁻	→	16	2	<i>A</i> ⁺	248885.48	248882.36	54.3	4.9	-3.2	1.89
	16	-3	<i>E</i>	→	15	-4	<i>E</i>	249192.86	249191.94	57.8	7.6	-5.9	0.44
	15	3	<i>A</i> ⁻	→	15	2	<i>A</i> ⁺	249419.90	249417.29	61.5	6.3	-3.9	2.80
	7	4	<i>A</i> ⁻	→	8	3	<i>A</i> ⁻	249443.34	249441.38	66.1	4.9	-4.6	1.86
	7	4	<i>A</i> ⁺	→	8	3	<i>A</i> ⁺	249451.89	249450.71	56.7	6.4	-5.6	1.80
	13	3	<i>A</i> ⁻	→	13	2	<i>A</i> ⁺	250291.13	250288.95	59.6	4.5	-4.4	2.65
	11	0	<i>A</i> ⁺	→	10	1	<i>A</i> ⁺	250507.02	250504.36	57.5	5.0	-3.8	2.15
	2	1	<i>E</i>	→	1	0	<i>E</i>	261805.74	261804.19	54.2	6.2	-5.2	1.24
	<i>J'</i>	<i>K'_a</i>	<i>K'_b</i>	→	<i>J''</i>	<i>K''_a</i>	<i>K''_b</i>						
CH ₂ NH	3	0	3	→	2	0	2	191462.82	191461.94	34.0	5.7	-5.6	0.26
	3	2	2	→	2	2	1	191959.30	191959.04	34.6	6.5	-6.6	0.15
	4	1	3	→	4	0	4	192212.32	192211.53	50.1	5.9	-5.8	0.26
	3	2	1	→	2	2	0	192469.59	192469.42	24.4	5.7	-6.7	0.16
	<i>J'</i>	<i>K'_a</i>	<i>Γ'</i>	→	<i>J''</i>	<i>K''_a</i>	<i>Γ''</i>						
CH ₃ NH ₂	14	2	<i>E</i> ₁₋₁	→	14	1	<i>E</i> ₁₊₁	192622.39	192621.18	28.4	5.0	-5.1	0.23
	16	2	<i>B</i> ₂	→	16	1	<i>B</i> ₁	193795.82	193795.24	28.7	5.2	-6.1	0.19
	3	1	<i>E</i> ₂₋₁	→	2	0	<i>E</i> ₂₊₁	202791.86	202792.09	11.0	4.0	-7.3	0.31
	12	2	<i>E</i> ₁₋₁	→	12	1	<i>E</i> ₁₊₁	203050.98	203050.54	33.3	6.3	-6.4	0.16
	3	2	<i>B</i> ₁	→	3	1	<i>B</i> ₂	248838.50	248839.64	29.2	7.6	-8.4	0.41
	2	2	<i>B</i> ₂	→	2	1	<i>B</i> ₁	250159.40	250160.03	55.3	6.9	-7.8	0.38
	12	1	<i>E</i> ₁₋₁	→	11	2	<i>E</i> ₁₊₁	250398.51	250399.29	7.4	3.3	-7.9	0.15
	4	1	<i>E</i> ₂₊₁	→	3	0	<i>E</i> ₂₊₁	261024.31	261024.77	15.6	4.1	-7.5	0.40
	4	1	<i>B</i> ₁	→	3	0	<i>B</i> ₂	261219.28	261219.25	49.2	8.6	-7.0	0.97
	8	0	<i>B</i> ₁	→	7	1	<i>B</i> ₂	261562.18	261562.72	47.2	8.3	-7.6	0.49
	4	1	<i>E</i> ₁₊₁	→	3	0	<i>E</i> ₁₊₁	264172.18	264171.58	49.2	7.3	-6.3	0.43
	9	2	<i>E</i> ₁₊₁	→	9	1	<i>E</i> ₁₋₁	264457.13	264455.82	29.1	6.8	-5.5	0.79

NOTE— The observed molecular transitions toward NGC6334I are summarized. T_{MB}, Δv, and V_{LSR} are, respectively, the brightness temperature, the FWHM line width, and the local standard of rest velocity. We showed the quantum number of CH₃OH, CH₃NH₂, and CH₂NH, respectively, the rest frequency, the observed frequency, and r.m.s noise level. The line parameters were obtained through the least-squares fitting assuming the shape of gaussian.

Table 8. Observed Lines towards NGC6334I MM2

Species	→						Rest. freq (MHz)	Obs freq (MHz)	T_{MB} (K)	Δv (km s ⁻¹)	V_{LSR} (km s ⁻¹)	rms (K)	
	J'	K'_a	Γ'	→	J''	K''_a	Γ''						
	6	3	E	→	7	2	E	191732.99	191733.87	77.0	6.2	-8.4	1.32
	4	1	A^+	→	3	1	A^+	191810.50	191811.46	75.5	6.5	-8.5	2.23
	4	0	E	→	3	0	E	193415.33	193416.28	74.3	7.1	-8.5	2.63
	4	-1	E	→	3	-1	E	193441.61	193442.54	66.3	7.7	-8.4	2.43
	4	0	A^+	→	3	0	A^+	193454.37	193455.50	68.8	7.4	-8.8	0.81
	4	1	E	→	3	1	E	193506.57	193507.85	77.1	7.4	-9.0	1.93
	1	1	A^+	→	2	0	A^+	205791.23	205792.37	80.7	6.2	-8.7	4.86
	18	3	A^-	→	18	2	A^+	247611.04	247611.93	86.7	5.7	-8.1	1.86
	23	1	E	→	23	0	E	247967.93	247969.04	55.1	4.3	-8.3	2.71
	16	3	A^-	→	16	2	A^+	248885.48	248886.37	82.1	5.8	-8.1	1.89
	16	-3	E	→	15	-4	E	249192.86	249193.89	60.6	5.2	-8.2	0.44
	15	3	A^-	→	15	2	A^+	249419.90	249420.86	82.0	6.3	-8.2	2.80
	7	4	A^-	→	8	3	A^-	249443.34	249444.49	71.2	5.8	-8.4	1.86
	7	4	A^+	→	8	3	A^+	249451.89	249453.00	71.2	6.3	-8.3	1.80
	13	3	A^-	→	13	2	A^+	250291.13	250292.01	80.6	7.3	-8.1	2.65
	11	0	A^+	→	10	1	A^+	250507.02	250508.32	61.2	7.8	-8.6	2.15
	2	1	E	→	1	0	E	261805.74	261807.05	71.8	6.9	-8.5	1.24
	J'	K'_a	K'_b	→	J''	K''_a	K''_b						
CH ₂ NH	3	0	3	→	2	0	2	191462.82	191463.43	5.8	4.1	-8.0	0.39
	3	2	2	→	2	2	1	191959.30	191959.52	2.6	3.7	-7.3	0.22
	4	1	3	→	4	0	4	192212.32	192213.20	12.3	3.9	-8.4	0.39
	3	2	1	→	2	2	0	192469.59	192470.21	2.9	3.0	-8.0	0.23
	7	1	6	→	7	0	7	250161.68	250162.08	10.5	4.6	-7.5	0.28
	J'	K'_a	Γ'	→	J''	K''_a	Γ''						
CH ₃ NH ₂	14	2	E_{1-1}	→	14	1	E_{1+1}	192622.39	192622.81	5.1	3.1	-7.7	0.34
	16	2	B_2	→	16	1	B_1	193795.82	193796.54	2.5	2.9	-8.1	0.28
	12	2	E_{1-1}	→	12	1	E_{1+1}	203050.98	203051.46	1.3	3.4	-7.7	0.24
	10	5	E_{2+1}	→	11	4	E_{2+1}	250110.22	250111.65	2.6	2.4	-8.7	0.31
	4	1	E_{2+1}	→	3	0	E_{2+1}	261219.28	261221.37	9.6	6.3	-9.4	0.94
	4	1	E_{1+1}	→	3	0	E_{1+1}	264172.18	264173.54	12.9	4.6	-8.5	2.65

NOTE— Same as Table 8 but toward NGC6334I MM2.

Table 9. Observed Lines towards NGC6334I MM3

Species	→						Rest. freq (MHz)	Obs freq (MHz)	T _{MB} (K)	Δv (km s ⁻¹)	V _{LSR} (km s ⁻¹)	rms (K)	
	<i>J'</i>	<i>K'_a</i>	<i>Γ'</i>	→	<i>J''</i>	<i>K''_a</i>	<i>Γ''</i>						
	6	3	<i>E</i>	→	7	2	<i>E</i>	191732.99	191733.87	77.0	6.2	-8.4	2.43
	4	1	<i>A</i> ⁺	→	3	1	<i>A</i> ⁺	191810.50	191811.46	75.5	6.5	-8.5	4.11
	4	0	<i>E</i>	→	3	0	<i>E</i>	193415.33	193416.28	74.3	7.1	-8.5	4.70
	4	-1	<i>E</i>	→	3	-1	<i>E</i>	193441.61	193442.54	66.3	7.7	-8.4	4.34
	4	0	<i>A</i> ⁺	→	3	0	<i>A</i> ⁺	193454.37	193455.50	68.8	7.4	-8.8	1.45
	4	1	<i>E</i>	→	3	1	<i>E</i>	193506.57	193507.85	77.1	7.4	-9.0	3.43
	1	1	<i>A</i> ⁺	→	2	0	<i>A</i> ⁺	205791.23	205792.37	80.7	6.2	-8.7	3.53
	18	3	<i>A</i> ⁻	→	18	2	<i>A</i> ⁺	247611.04	247611.93	86.7	5.7	-8.1	0.67
	16	3	<i>A</i> ⁻	→	16	2	<i>A</i> ⁺	248885.48	248886.37	82.1	5.8	-8.1	0.40
	16	-3	<i>E</i>	→	15	-4	<i>E</i>	249192.86	249193.89	60.6	5.2	-8.2	0.29
	15	3	<i>A</i> ⁻	→	15	2	<i>A</i> ⁺	249419.90	249420.86	82.0	6.3	-8.2	0.69
	7	4	<i>A</i> ⁻	→	8	3	<i>A</i> ⁻	249443.34	249444.49	71.2	5.8	-8.4	0.57
	7	4	<i>A</i> ⁺	→	8	3	<i>A</i> ⁺	249451.89	249453.00	71.2	6.3	-8.3	0.65
	13	3	<i>A</i> ⁻	→	13	2	<i>A</i> ⁺	250291.13	250292.01	80.6	7.3	-8.1	0.77
	2	1	<i>E</i>	→	1	0	<i>E</i>	261805.74	261807.05	71.8	6.9	-8.5	0.66
	<i>J'</i>	<i>K'_a</i>	<i>K'_b</i>	→	<i>J''</i>	<i>K''_a</i>	<i>K''_b</i>						
CH ₂ NH	3	0	3	→	2	0	2	191462.82	191464.20	0.6	2.6	-9.2	0.72
	3	2	2	→	2	2	1	191959.30	191961.06	0.5	3.6	-9.7	0.41
	4	1	3	→	4	0	4	192212.32	192213.72	0.7	3.1	-9.2	0.70
	3	2	1	→	2	2	0	192469.59	192470.84	0.5	3.0	-8.9	0.42

NOTE— Same as Table 7 but toward NGC6334I MM3.

Table 10. Observed Lines towards G10.47+0.03

Species	→						Rest. freq (MHz)	Obs freq (MHz)	T_{MB} (K)	Δv (km s ⁻¹)	V_{LSR} (km s ⁻¹)	rms (K)	
	J'	K'_a	Γ'	→	J''	K''_a	Γ''						
CH ₃ OH	6	3	E	→	7	2	E	191732.99	191734.01	69.3	11.1	65.4	3.43
	4	1	A^+	→	3	1	A^+	191810.50	191811.63	69.0	12.9	65.2	1.14
	4	0	E	→	3	0	E	193415.33	193417.12	68.5	12.2	64.2	0.73
	4	-1	E	→	3	-1	E	193441.61	193443.24	61.8	9.8	64.5	1.35
	4	0	A^+	→	3	0	A^+	193454.37	193456.95	61.9	11.4	63.0	1.35
	4	1	E	→	3	1	E	193506.57	193506.82	58.7	10.9	66.6	1.46
	1	1	A^+	→	2	0	A^+	205791.23	205792.69	55.5	12.0	64.9	0.21
	18	3	A^-	→	18	2	A^+	247611.04	247612.26	69.4	14.2	65.5	2.07
	23	1	E	→	23	0	E	247967.93	247969.58	53.6	9.4	65.0	1.19
	16	3	A^-	→	16	2	A^+	248885.48	248886.58	71.2	10.0	65.7	2.07
	16	-3	E	→	15	-4	E	249192.86	249194.14	53.8	11.3	65.5	0.59
	15	3	A^-	→	15	2	A^+	249419.90	249420.85	80.1	10.4	65.9	2.67
	7	4	A^-	→	8	3	A^-	249443.34	249443.69	56.2	9.7	66.6	2.07
	7	4	A^+	→	8	3	A^+	249451.89	249453.19	56.8	10.4	65.4	2.37
	13	3	A^-	→	13	2	A^+	250291.13	250292.50	80.1	11.2	65.4	2.67
11	0	A^+	→	10	1	A^+	250507.02	250508.50	56.5	8.9	65.2	2.67	
2	1	E	→	1	0	E	261805.74	261807.91	55.7	9.5	64.5	3.85	
	J'	K'_a	K'_b	→	J''	K''_a	K''_b						
CH ₂ NH	3	0	3	→	2	0	2	191462.82	191462.67	25.3	11.1	67.2	0.10
	3	2	2	→	2	2	1	191959.30	191959.61	14.8	8.0	66.5	0.10
	4	1	3	→	4	0	4	192212.32	192212.82	29.8	9.0	66.2	0.31
	3	2	1	→	2	2	0	192469.59	192469.59	11.9	9.1	67.0	0.21
	7	1	6	→	7	0	7	250161.68	250162.00	39.3	9.2	66.6	1.19
	J'	K'_a	K'_b	→	J''	K''_a	K''_b						
CH ₃ NH ₂	11	1	B_2	→	10	2	B_1	260963.40	260963.40	15.4	7.3	67.0	0.89
	4	1	E_{2+1}	→	3	0	E_{2+1}	261024.31	261023.82	11.5	5.4	67.6	0.59
	4	1	B_1	→	3	0	B_2	261219.28	261220.78	18.0	8.4	65.3	0.89
	8	0	B_1	→	7	1	B_2	261562.18	261564.24	33.8	10.9	64.6	0.69
	4	1	E_{1+1}	→	3	0	E_{1+1}	264172.18	264172.89	40.8	10.7	66.2	0.69

NOTE— Same as Table 7 but toward G10.47+0.03.

Table 11. Observed Lines towards G31.41+0.3

Species	→						Rest. freq (MHz)	Obs freq (MHz)	T _{MB} (K)	Δv (km s ⁻¹)	V _{LSR} (km s ⁻¹)	rms (K)	
	<i>J'</i>	<i>K'_a</i>	<i>Γ'</i>	→	<i>J''</i>	<i>K''_a</i>	<i>Γ''</i>						
CH ₃ OH	6	3	<i>E</i>	→	7	2	<i>E</i>	191732.99	191733.95	47.1	10.9	95.5	0.45
	18	3	<i>A</i> ⁻	→	18	2	<i>A</i> ⁺	247611.04	247610.99	49.9	10.5	97.1	0.60
	23	1	<i>E</i>	→	23	0	<i>E</i>	247967.93	247967.96	33.9	7.7	97.0	0.39
	16	3	<i>A</i> ⁻	→	16	2	<i>A</i> ⁺	248885.48	248885.37	53.0	10.2	97.1	0.60
	16	-3	<i>E</i>	→	15	-4	<i>E</i>	249192.86	249193.20	37.9	9.8	96.6	0.42
	15	3	<i>A</i> ⁻	→	15	2	<i>A</i> ⁺	249419.90	249420.04	53.6	10.1	96.8	0.19
	7	4	<i>A</i> ⁻	→	8	3	<i>A</i> ⁻	249443.34	249443.38	47.7	8.6	97.0	0.42
	7	4	<i>A</i> ⁺	→	8	3	<i>A</i> ⁺	249451.89	249452.04	44.4	7.0	96.8	0.78
	13	3	<i>A</i> ⁻	→	13	2	<i>A</i> ⁺	250291.13	250291.06	56.5	9.8	97.1	0.93
	11	0	<i>A</i> ⁺	→	10	1	<i>A</i> ⁺	250507.02	250507.24	50.5	9.3	96.7	1.69
		<i>J'</i>	<i>K'_a</i>	<i>K'_b</i>	→	<i>J''</i>	<i>K''_a</i>	<i>K''_b</i>					
CH ₂ NH	3	0	3	→	2	0	2	191462.82	191463.20	14.7	7.6	96.4	0.27
	3	2	2	→	2	2	1	191959.30	191959.39	12.7	6.5	96.9	0.06
	4	1	3	→	4	0	4	192212.32	192212.40	24.0	7.4	96.9	0.25
	3	2	1	→	2	2	0	192469.59	192469.67	13.0	6.7	96.9	0.15
	7	1	6	→	7	0	7	250161.68	250161.13	31.6	8.0	97.7	0.42
	<i>J'</i>	<i>K'_a</i>	<i>Γ'</i>	→	<i>J''</i>	<i>K''_a</i>	<i>Γ''</i>						
CH ₃ NH ₂	12	2	<i>E</i> ₁₋₁	→	12	1	<i>E</i> ₁₊₁	203050.98	203050.53	5.0	8.6	97.7	0.18
	3	2	<i>B</i> ₁	→	3	1	<i>B</i> ₂	248838.50	248840.06	15.6	7.3	95.1	0.39
	4	2	<i>A</i> ₁	→	4	1	<i>A</i> ₂	250110.22	250110.06	7.6	5.8	97.2	0.20
	12	1	<i>E</i> ₁₋₁	→	11	2	<i>E</i> ₁₊₁	250398.51	250399.89	9.7	8.6	95.3	0.26
	4	1	<i>E</i> ₂₊₁	→	3	0	<i>E</i> ₂₊₁	261024.31	261023.38	10.7	6.8	98.1	0.26
	4	1	<i>B</i> ₁	→	3	0	<i>B</i> ₂	261219.28	261219.99	19.1	7.7	96.2	0.45
	8	0	<i>B</i> ₁	→	7	1	<i>B</i> ₂	261562.18	261563.50	37.8	9.9	95.5	0.75
	4	1	<i>E</i> ₁₊₁	→	3	0	<i>E</i> ₁₊₁	264172.18	264173.14	22.1	10.3	95.9	0.75

NOTE— Same as Table 8 but toward G31.41+0.3.

Table 12. Observed Lines towards W51 e2

Species	→						Rest. freq (MHz)	Obs freq (MHz)	T_{MB} (K)	Δv (km s ⁻¹)	V_{LSR} (km s ⁻¹)	rms (K)	
	J'	K'_a	Γ'	→	J''	K''_a	Γ''						
CH ₃ OH	6	3	E	→	7	2	E	191732.99	191731.90	35.9	5.4	58.7	0.74
	4	1	A^+	→	3	1	A^+	191810.50	191809.38	37.2	4.7	58.8	2.40
	4	0	E	→	3	0	E	193415.33	193413.94	43.9	5.5	59.2	0.96
	4	-1	E	→	3	-1	E	193441.61	193440.30	42.2	5.4	59.0	2.97
	4	0	A^+	→	3	0	A^+	193454.37	193452.95	41.2	5.5	59.2	3.08
	4	1	E	→	3	1	E	193506.57	193505.20	46.6	5.7	59.1	1.94
	1	1	A^+	→	2	0	A^+	205791.23	205790.03	37.6	5.0	58.7	1.71
	13	3	A^-	→	13	2	A^+	250291.13	250289.38	28.8	5.1	59.1	3.59
	11	0	A^+	→	10	1	A^+	250507.02	250504.85	28.6	5.1	59.6	4.70
	2	1	E	→	1	0	E	261805.74	261804.15	39.5	4.7	58.8	3.87
	J'	K'_a	K'_b	→	J''	K''_a	K''_b						
CH ₂ NH	3	0	3	→	2	0	2	191462.82	191463.12	5.0	7.0	56.5	0.42
	3	2	2	→	2	2	1	191959.30	191960.24	4.6	6.0	55.5	0.14
	4	1	3	→	4	0	4	192212.32	192213.30	11.2	6.3	55.5	0.37
	3	2	1	→	2	2	0	192469.59	192470.51	3.8	4.8	55.6	0.15
	7	1	6	→	7	0	7	250161.68	250162.38	13.6	5.7	56.2	0.94
	J'	K'_a	Γ'	→	J''	K''_a	Γ''						
CH ₃ NH ₂	16	2	B_2	→	16	1	B_1	193795.82	193796.61	3.7	4.8	55.8	0.05
	12	2	E_{1-1}	→	12	1	E_{1+1}	203050.98	203051.55	4.0	7.5	56.2	0.13
	4	2	A_1	→	4	1	A_2	250110.22	250111.74	4.6	4.9	55.2	0.21
	4	1	E_{2+1}	→	3	0	E_{2+1}	261024.31	261023.80	5.1	2.9	57.6	0.72
	8	0	B_1	→	7	1	B_2	261562.18	261562.24	21.0	6.1	56.9	0.85
4	1	E_{1+1}	→	3	0	E_{1+1}	264172.18	264173.94	22.2	7.5	55.0	0.97	

NOTE— Same as Table 8 but toward W51 e2.

Table 13. Observed Lines towards W51 e8

Species	→						Rest. freq (MHz)	Obs freq (MHz)	T _{MB} (K)	Δv (km s ⁻¹)	V _{LSR} (km s ⁻¹)	rms (K)	
	<i>J'</i>	<i>K'_a</i>	<i>Γ'</i>	→	<i>J''</i>	<i>K''_a</i>	<i>Γ''</i>						
CH ₃ OH	6	3	<i>E</i>	→	7	2	<i>E</i>	191732.99	191732.82	36.6	9.5	57.3	0.59
	4	1	<i>A</i> ⁺	→	3	1	<i>A</i> ⁺	191810.50	191810.43	50.3	10.3	57.1	0.77
	4	0	<i>E</i>	→	3	0	<i>E</i>	193415.33	193415.16	49.0	10.6	57.3	0.54
	4	-1	<i>E</i>	→	3	-1	<i>E</i>	193441.61	193441.01	41.3	9.6	57.9	0.64
	4	0	<i>A</i> ⁺	→	3	0	<i>A</i> ⁺	193454.37	193454.10	43.7	11.4	57.4	0.96
	4	1	<i>E</i>	→	3	1	<i>E</i>	193506.57	193506.70	51.9	10.9	56.8	0.46
	1	1	<i>A</i> ⁺	→	2	0	<i>A</i> ⁺	205791.23	205791.15	33.5	8.3	57.1	1.60
	18	3	<i>A</i> ⁻	→	18	2	<i>A</i> ⁺	247611.04	247610.79	48.9	10.4	57.3	0.50
	23	1	<i>E</i>	→	23	0	<i>E</i>	247967.93	247967.76	15.3	10.2	57.2	0.39
	16	3	<i>A</i> ⁻	→	16	2	<i>A</i> ⁺	248885.48	248885.00	53.7	9.5	57.6	0.50
	16	-3	<i>E</i>	→	15	-4	<i>E</i>	249192.86	249192.67	28.3	10.0	57.2	0.36
	15	3	<i>A</i> ⁻	→	15	2	<i>A</i> ⁺	249419.90	249420.20	44.7	8.7	56.6	0.17
	7	4	<i>A</i> ⁻	→	8	3	<i>A</i> ⁻	249443.34	249443.45	34.5	9.5	56.9	0.39
	7	4	<i>A</i> ⁺	→	8	3	<i>A</i> ⁺	249451.89	249452.09	30.5	7.8	56.8	0.30
13	3	<i>A</i> ⁻	→	13	2	<i>A</i> ⁺	250291.13	250290.71	55.6	9.8	57.5	0.97	
11	0	<i>A</i> ⁺	→	10	1	<i>A</i> ⁺	250507.02	250507.03	45.6	9.6	57.0	0.83	
2	1	<i>E</i>	→	1	0	<i>E</i>	261805.74	261806.50	38.5	7.4	56.1	2.38	
	<i>J'</i>	<i>K'_a</i>	<i>K'_b</i>	→	<i>J''</i>	<i>K''_a</i>	<i>K''_b</i>						
CH ₂ NH	3	0	3	→	2	0	2	191462.82	191461.44	8.5	9.5	59.2	0.31
	3	2	2	→	2	2	1	191959.30	191957.43	5.3	7.5	59.9	0.05
	4	1	3	→	4	0	4	192212.32	192210.28	13.6	10.4	60.2	0.26
	3	2	1	→	2	2	0	192469.59	192467.57	4.5	6.0	60.1	0.07
	7	1	6	→	7	0	7	250161.68	250159.51	16.4	9.4	59.6	0.44
	<i>J'</i>	<i>K'_a</i>	<i>Γ'</i>	→	<i>J''</i>	<i>K''_a</i>	<i>Γ''</i>						
CH ₃ NH ₂	16	2	<i>B</i> ₂	→	16	1	<i>B</i> ₁	193795.82	193793.48	4.7	4.9	60.6	0.03
	12	2	<i>E</i> ₁₋₁	→	12	1	<i>E</i> ₁₊₁	203050.98	203048.30	3.3	6.8	61.0	0.07
	12	1	<i>E</i> ₁₋₁	→	11	2	<i>E</i> ₁₊₁	250398.51	250396.18	2.0	8.3	59.8	0.25
	11	1	<i>B</i> ₂	→	10	2	<i>B</i> ₁	260963.40	260960.81	9.9	8.9	60.0	0.41
	4	1	<i>E</i> ₂₊₁	→	3	0	<i>E</i> ₂₊₁	261024.31	261021.35	4.3	4.3	60.4	0.17
	4	1	<i>B</i> ₁	→	3	0	<i>B</i> ₂	261219.28	261217.24	8.3	7.1	59.3	0.41
	6	2	<i>B</i> ₁	→	6	1	<i>B</i> ₂	261252.83	261251.72	27.8	10.8	58.3	0.61
	8	0	<i>B</i> ₁	→	7	1	<i>B</i> ₂	261562.18	261558.15	4.7	5.9	61.6	0.19
	4	1	<i>E</i> ₁₊₁	→	3	0	<i>E</i> ₁₊₁	264172.18	264170.05	12.7	7.8	59.4	0.44

NOTE— Same as Table 8 but toward W51 e8.

Table 14. CH₃NH₂ Lines towards Orion KL Hot core from Archival Data

Species	→						Rest. freq (MHz)	Obs freq (MHz)	E _u (K)	Sμ ² (D ²)	T _{MB} (K)	Δv (km s ⁻¹)	V _{LSR} (km s ⁻¹)	rms (K)	
	<i>J'</i>	<i>K'_a</i>	<i>Γ'</i>	→	<i>J''</i>	<i>K''_a</i>	<i>Γ''</i>								
CH ₃ NH ₂	12	2	<i>B</i> ₂	→	12	1	<i>B</i> ₁	217758.43	217758.23	182.1	10.8	0.86	4.0	4.7	0.034
	8	2	<i>A</i> ₂	→	8	1	<i>A</i> ₁	229908.19	229908.12	92.7	6.8	0.65	3.2	4.9	0.064
	8	2	<i>B</i> ₂	→	8	1	<i>B</i> ₁	235735.08	235734.97	92.8	6.8	1.70	5.6	4.9	0.081
	6	2	<i>B</i> ₂	→	6	1	<i>B</i> ₁	242262.12	242261.96	60.9	5.0	2.03	8.0	4.8	0.166
	5	2	<i>B</i> ₁	→	5	1	<i>B</i> ₂	244886.67	244886.86	48.1	4.1	1.29	4.2	5.2	0.043
	12	1	<i>B</i> ₂	→	11	2	<i>B</i> ₁	245202.56	245202.16	168.3	3.2	0.37	3.9	4.5	0.037

Table 15. The Derived Abundance

Source	N[H ₂] (cm ⁻²)	N[CH ₃ OH] (cm ⁻²)	T _{ex} [CH ₃ OH] (K)	N[CH ₃ NH ₂] (cm ⁻²)	T _{ex} [CH ₃ NH ₂] (K)	N[CH ₂ NH] (cm ⁻²)	T _{ex} [CH ₂ NH] (K)
NGC6334I MM1	1.8 (25)	4.5 ± 1.8 (17)	120 ± 32	1.0 ± 0.1 (18)	120 ± 11	8.6 ± 4.8 (16)	[120]
NGC6334I MM2	1.2 (24)	6.5 ± 1.8 (17)	157 ± 36	6.8 ± 2.3 (16)	91 ± 16	8.7 ± 1.2 (15)	137 ± 46
NGC6334I MM3	1.8 (24)	6.2 ± 1.9 (17)	169 ± 47	< 1.0 (16)	[170]	9.3 ± 5.4 (14)	[170]
G10.47+0.03	6.3 (24)	1.3 ± 0.4 (18)	235 ± 71	9.4 ± 2.7 (17)	166 ± 106	5.3 ± 1.2 (16)	90 ± 31
G31.41+0.3	7.5 (24)	8.3 ± 3.7 (17)	207 ± 55	3.2 ± 0.7 (17)	79 ± 18	7.4 ± 1.8 (16)	184 ± 141
W51 e2	9.1 (24)	1.3 ± 0.3 (17)	94 ± 19	1.9 ± 0.4 (17)	95 ± 14	1.9 ± 0.4 (16)	155 ± 98
W51 e8	4.1 (24)	6.5 ± 1.6 (17)	205 ± 40	2.5 ± 1.1 (17)	131 ± 51	2.7 ± 0.3 (16)	130 ± 28

NOTE— The column density of molecular hydrogen, and the column densities and the excitation temperatures for CH₃OH, CH₃NH₂, and CH₂NH derived by the rotaton diagram method are shown. For CH₂NH in NGC6334I MM1 and MM3, excitation temperatures are assumed as they are shown in brackets. The upper limit of CH₃NH₂ column density is shown for NGC6334I MM3. a (b) means a × 10^b.

Table 16. Comparison with Chemical Model

Source	CH ₃ NH ₂ /CH ₃ OH obs	X[CH ₃ OH] obs	X[CH ₃ NH ₂] obs	X[CH ₂ NH] obs
NGC6334I MM1	2.2 ± 1.0	1.2 (-8)	2.8 (-8)	9.4 (-10)
NGC6334I MM2	0.11 ± 0.05	1.2 (-7)	2.8 (-8)	3.6 (-9)
NGC6334I MM3	<0.02	1.7 (-7)	<2.9 (-9)	2.6 (-10)
G10.47+0.03	0.72 ± 0.32	1.0 (-7)	7.5 (-8)	4.2 (-9)
G31.41+0.3	0.39 ± 0.19	5.3 (-8)	2.1 (-8)	4.9 (-9)
W51 e2	1.4 ± 0.5	7.2 (-9)	1.0 (-8)	1.0 (-9)
W51 e8	0.38 ± 0.19	8.0 (-8)	3.1 (-8)	3.3 (-9)
Model	CH ₃ NH ₂ /CH ₃ OH			
Our standard model	0.19-0.39			
B=0.7	0.49-1.0			
B=0.2	1.0-9.4			
B=0.1	1.0-75			
T=200 K	0.20-0.32			
n=1×10 ⁶ cm ⁻²	0.14-0.18			
n=1×10 ⁸ cm ⁻²	0.15-0.17			
long warm up	0.11-0.35			
short warm up	0.09-0.10			
Garrod (Fast)	0.007			
Garrod (Medium)	0.004			
Garrod (Slow)	0.001			
Previous Study	CH ₃ NH ₂ /CH ₃ OH			
Sgr B2(M) ^a	8.0×10 ⁻³			
Sgr B2(N) ^a	0.03			
Sgr B2(N) ^b	0.10			
NGC6334I MM1 ^c	(2.5-5.9)×10 ⁻³			
NGC6334I MM2 ^c	(0.9-1.5)×10 ⁻³			
NGC6334I MM3 ^c	(4.8-5.4)×10 ⁴			
IRAS 16293-2422B ^d	<5.3×10 ⁻⁵			

NOTE— (Top) The observed abundance ratios of CH₃NH₂/CH₃OH is shown. X[CH₃OH], X[CH₃NH₂], and X[CH₂NH], respectively, are the fractional abundances of CH₃OH, CH₃NH₂, and CH₂NH, which are derived by dividing their column densities by that of molecular hydrogen column density. (Middle) The predictions of these molecular ratios by chemical modeling are also summarized. The age of the simulation is constrained so that the observed fractional abundances of CH₃OH and CH₃NH₂ are explained within a factor of 10. For comparison, the peak abundance ratios under three warm-up models presented by Garrod (2013) are also shown. (Bottom) The observed abundance ratios of “CH₃NH₂/CH₃OH” and “CH₃NH₂/CH₃OH” from the previous studies. Citation: (a) Belloche et al. (2013), (b) Neill et al. (2014), (c) Bøgelund et al. (2019) (d) Ligterink et al. (2018)

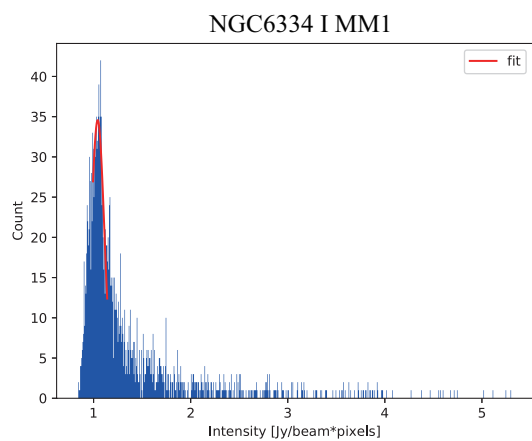


Figure 1. An example of the intensity histogram obtained in NGC6334I MM1 region. The Gaussian fitting is performed to obtain the mean and the standard deviation, which are used to subtract the continuum emission with casa.

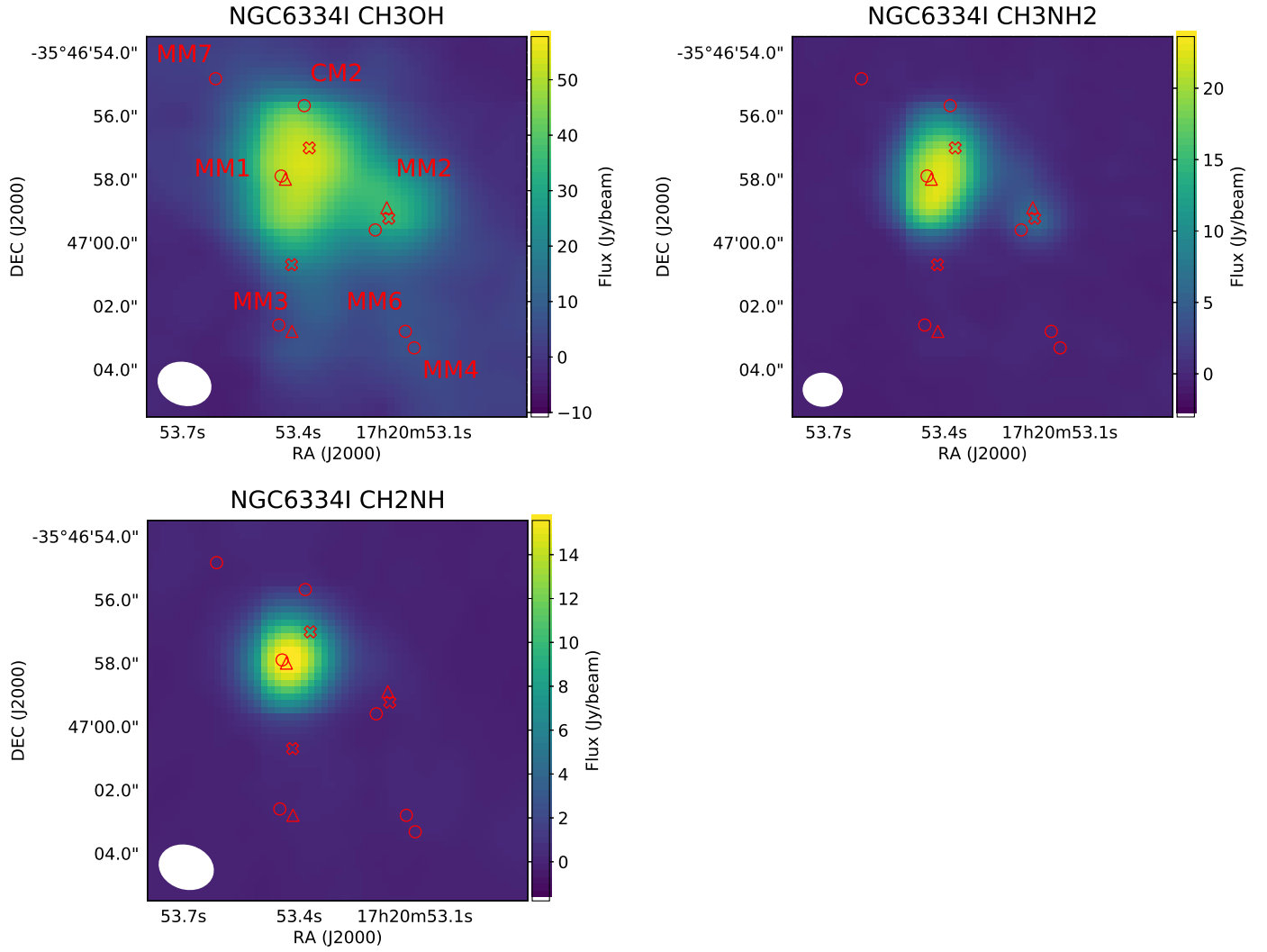


Figure 2. The integrated intensity maps of CH₃OH $4, 1, E \rightarrow 3, 1, E$, CH₃NH₂ $4, 1, E_{1+1} \rightarrow 3, 0, E_{1+1}$, and CH₂NH $3, 2, 2 \rightarrow 2, 2, 1$ transition toward NGC6334I. The positions of previously known continuum sources (Hunter et al. 2006; Brogan et al. 2016) are shown by circles on the map. The triangles shows the positions of hot cores, MM1, MM2, and MM3, where the spectra was extracted. The positions observed by Bøgelund et al. (2019) are marked by X position. The velocity ranges are from -14.6 to -0.9, from -14.2 to -5.9, and from -13.9 to -0.2 km s⁻¹ for CH₃OH, CH₃NH₂, and CH₂NH, respectively.

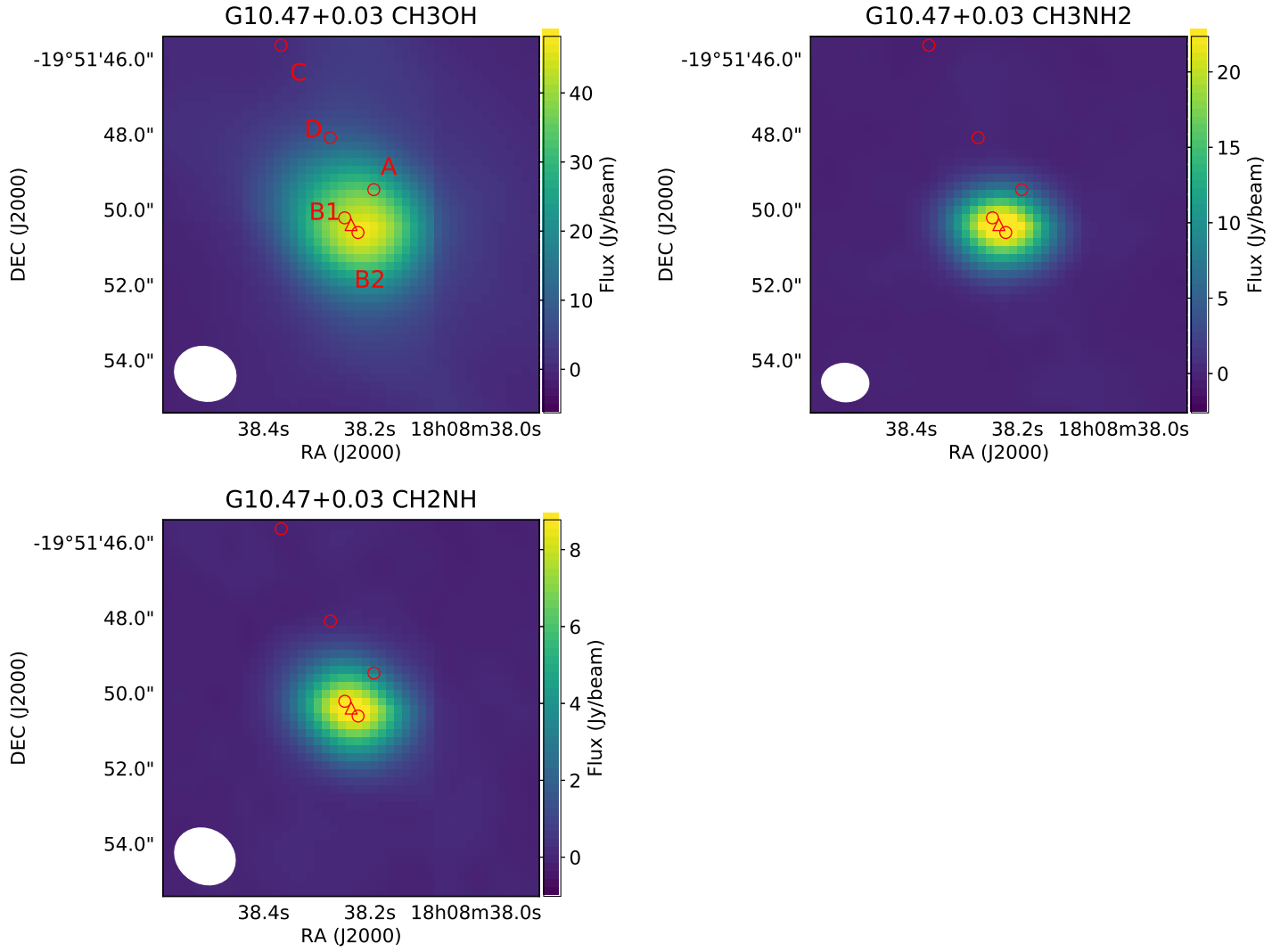


Figure 3. The integrated intensity maps of CH₃OH $4, 1, E \rightarrow 3, 1, E$, CH₃NH₂ $4, 1, E_{1+1} \rightarrow 3, 0, E_{1+1}$, and CH₂NH $3, 2, 2 \rightarrow 2, 2, 1$ transition toward G10.41+0.03. The positions of previously known continuum sources (Wood & Churchwell 1989; Cesaroni et al. 1998, 2010) are shown by circles on the map. The triangle shows the position of hot core, where the spectra was extracted. The velocity ranges are from 57.6 to 71.3, from 58.8 to 67.1, and from 62.9 to 76.6 km s⁻¹ for CH₃OH, CH₃NH₂, and CH₂NH, respectively.

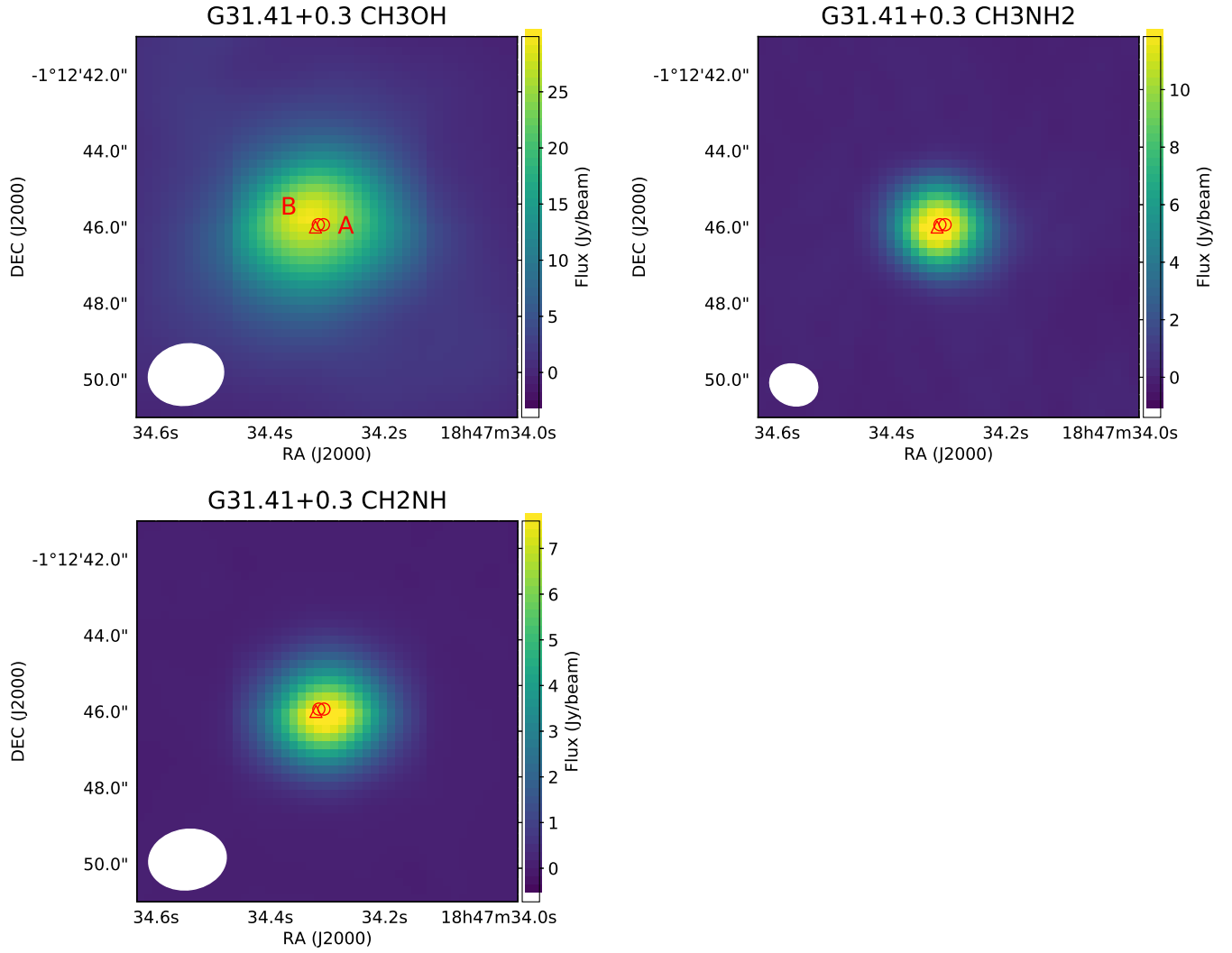


Figure 4. The integrated intensity maps of CH₃OH $4, 1, E \rightarrow 3, 1, E$, CH₃NH₂ $4, 1, E_{1+1} \rightarrow 3, 0, E_{1+1}$, and CH₂NH $3, 2, 2 \rightarrow 2, 2, 1$ transition toward G31.41+0.3. The positions of previously known continuum sources (Cesaroni et al. 2010) are shown by circles on the map. The triangle shows the position of hot core, where the spectra was extracted. The velocity ranges are from 85.6 to 99.2, from 89.8 to 98.1, and from 90.8 to 104.5 km s⁻¹ for CH₃OH, CH₃NH₂, and CH₂NH, respectively.

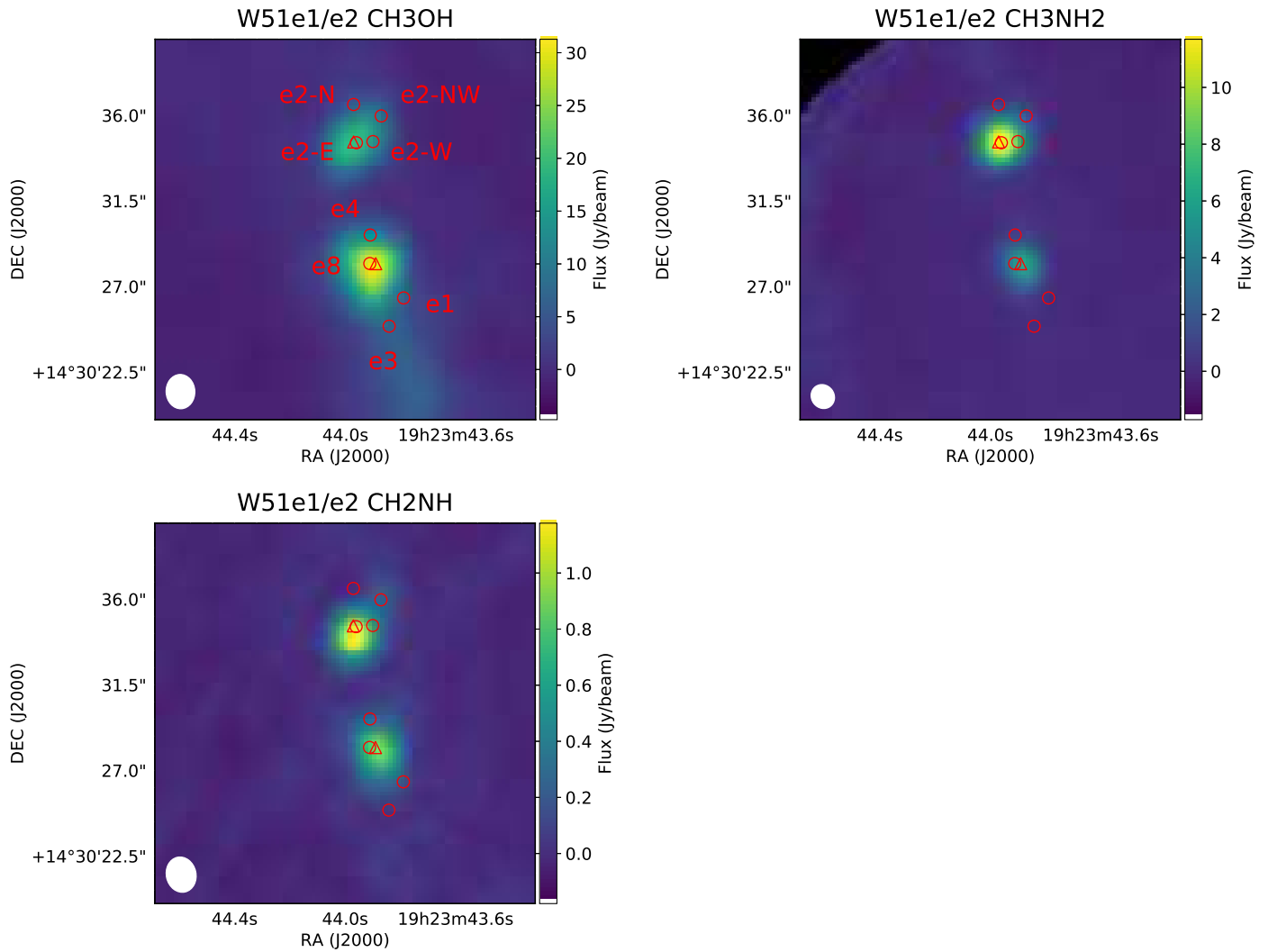


Figure 5. The integrated intensity maps of CH₃OH 4, 1, *E* → 3, 1, *E*, CH₃NH₂ 4, 1, *E*₁₊₁ → 3, 0, *E*₁₊₁, and CH₂NH 3, 2, 2 → 2, 2, 1 transition toward W51 e1/e2. The positions of previously known continuum sources (Gaume et al. 1993; Shi et al. 2010) are shown on the map by circles. The triangles shows the positions of hot cores, where the spectra was extracted. The velocity ranges are from 44.9 to 58.5, from 49.8 to 58.1, and from 47.0 to 60.7 km s⁻¹ for CH₃OH, CH₃NH₂, and CH₂NH, respectively.

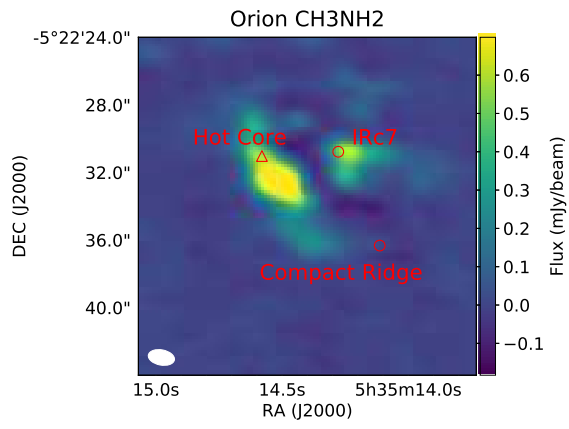


Figure 6. Integrated intensity map of CH_3NH_2 $5, 2, B_1 \rightarrow 5, 1, B_2$ transition toward Orion KL. The triangle shows the positions of the Orion Hot core, where the spectra was extracted. The circles denote the positions of IRc7, and Compact ridge. The velocity range is from 3.0 to 12.0 km s^{-1} .

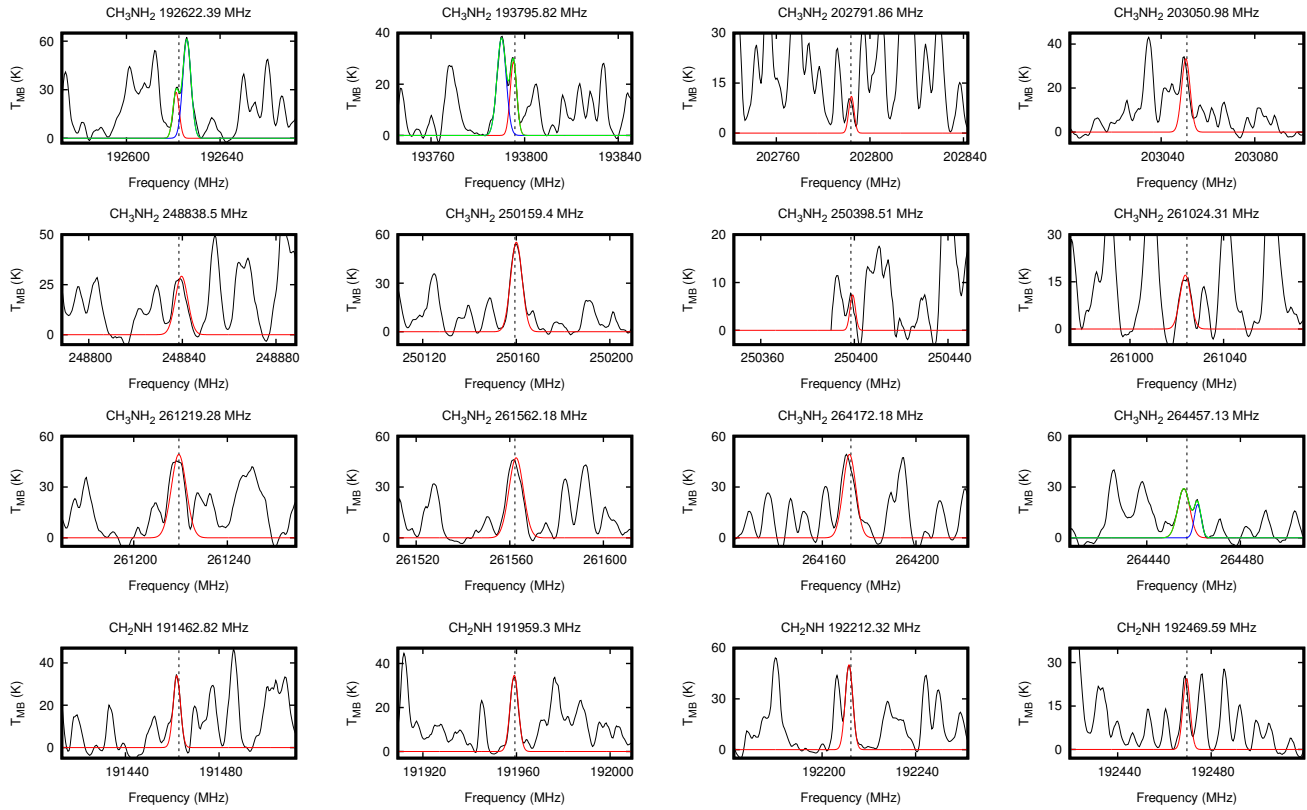


Figure 7. The observed transitions of CH₃NH₂ and CH₂NH toward NGC6334I MM1 at the position in . T_{rMB} is the brightness temperature. The vertical dotted lines represent the rest frequency calculated from the velocity of source. The results of Gaussian fitting is overlapped on the spectra with red line. For some cases, we performed least-squares fitting assuming more than two components of Gaussian, and other Gaussian components and the shape of the sum of all Gaussians are shown by blue lines.

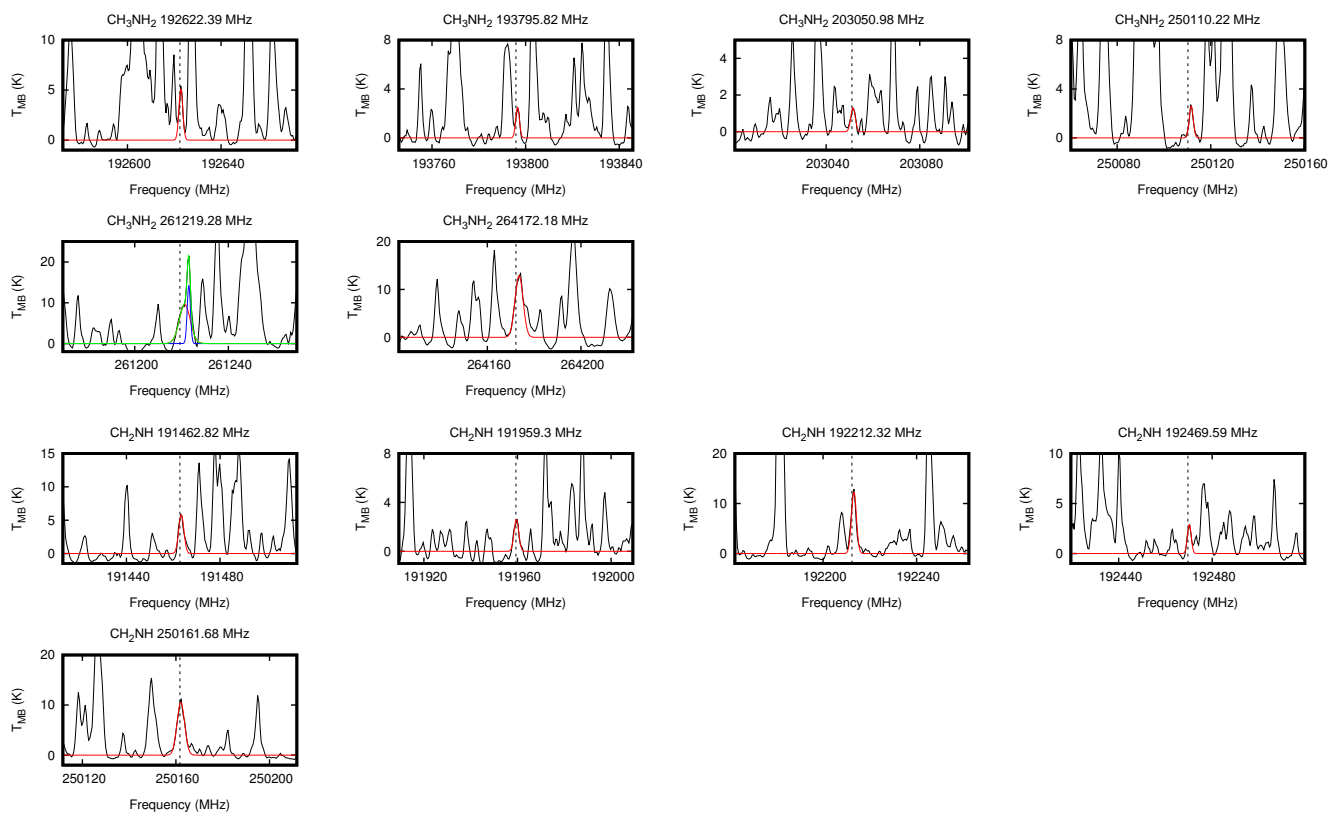


Figure 8. The same as Figure 7 but toward NGC6334I MM2.

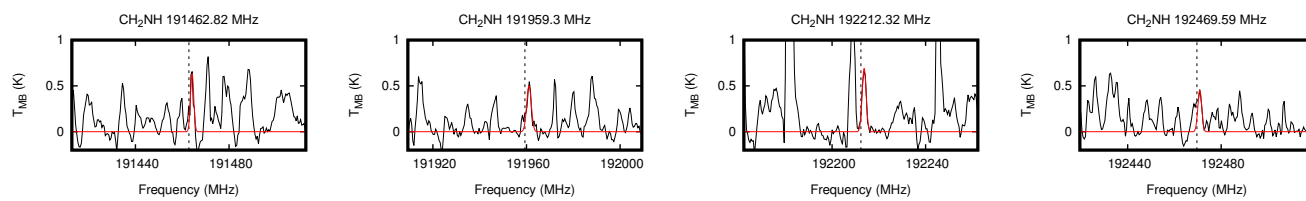


Figure 9. The same as Figure 7 but toward NGC6334I MM3.

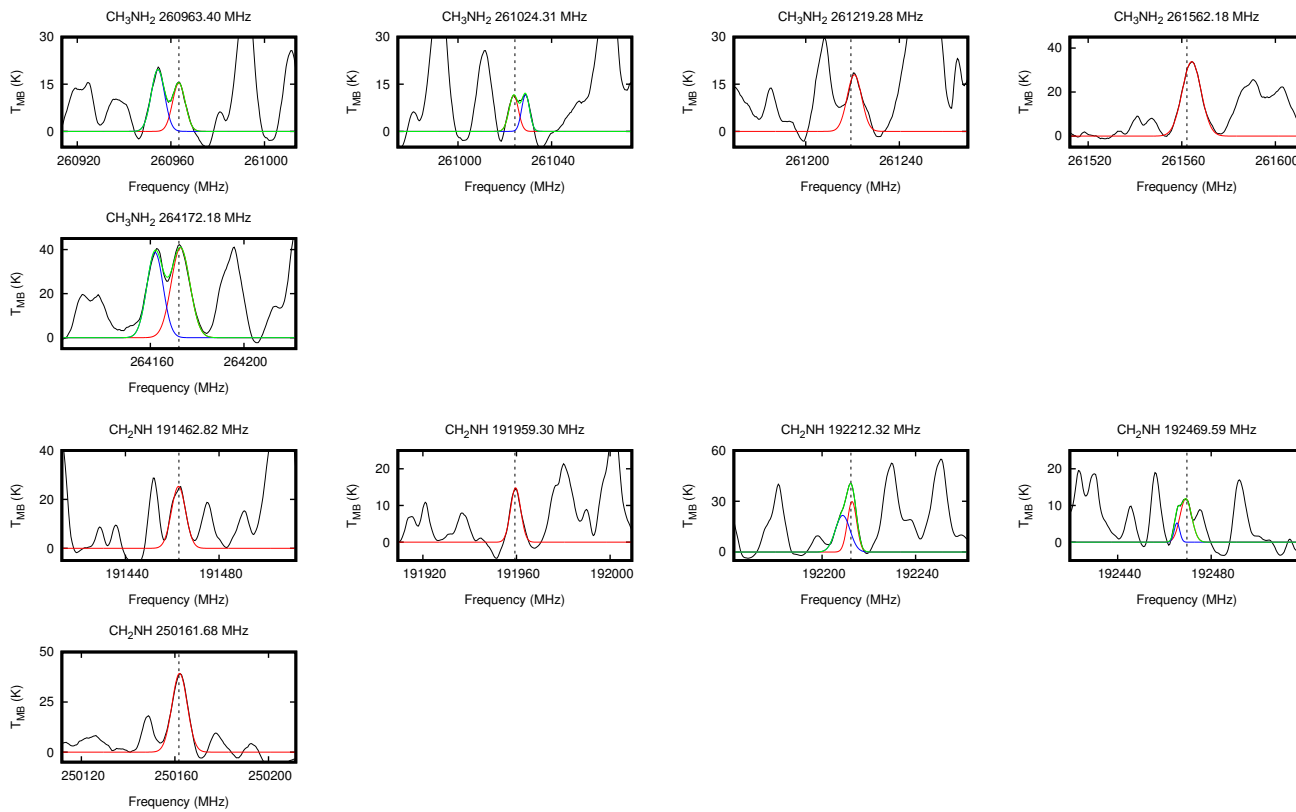


Figure 10. The same as Figure 7 but toward G10.47+0.03.

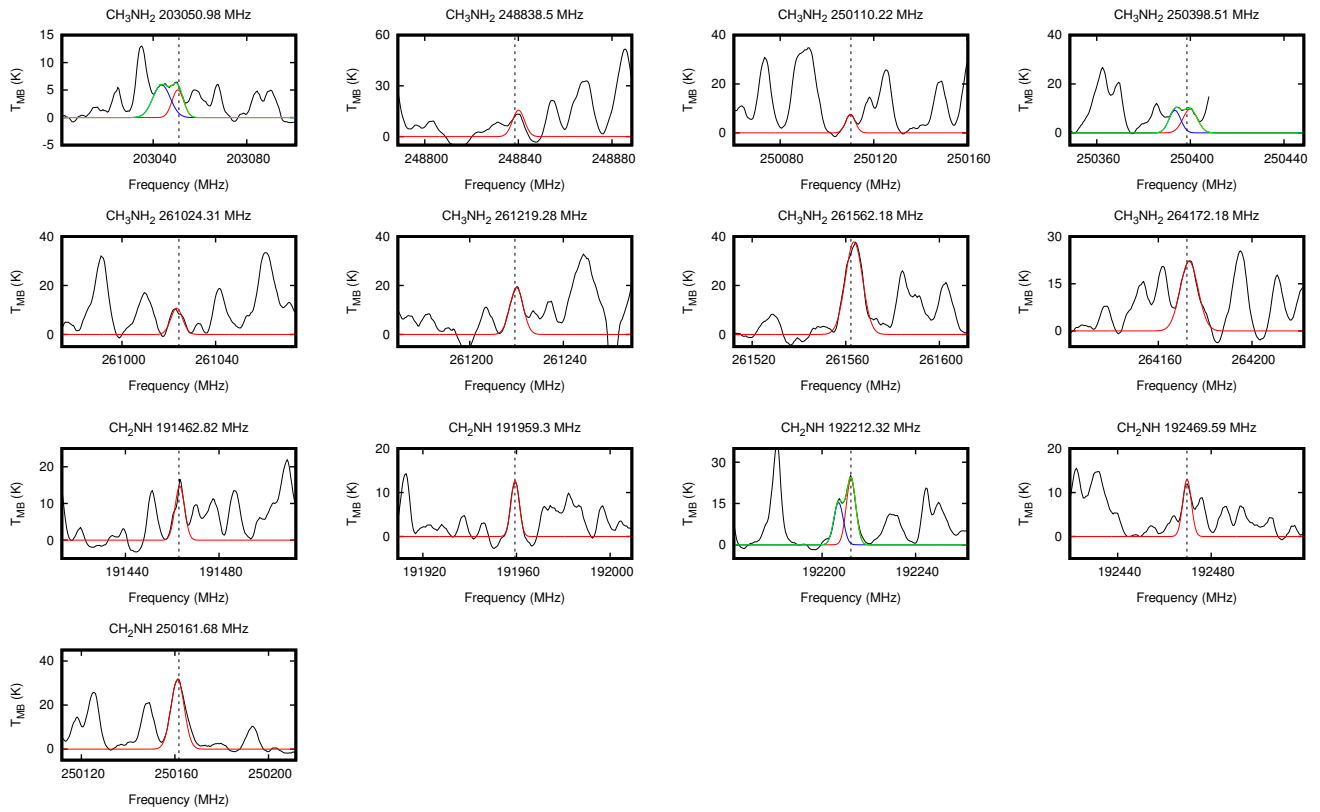


Figure 11. The same as Figure 7 but toward G31.41+0.3.

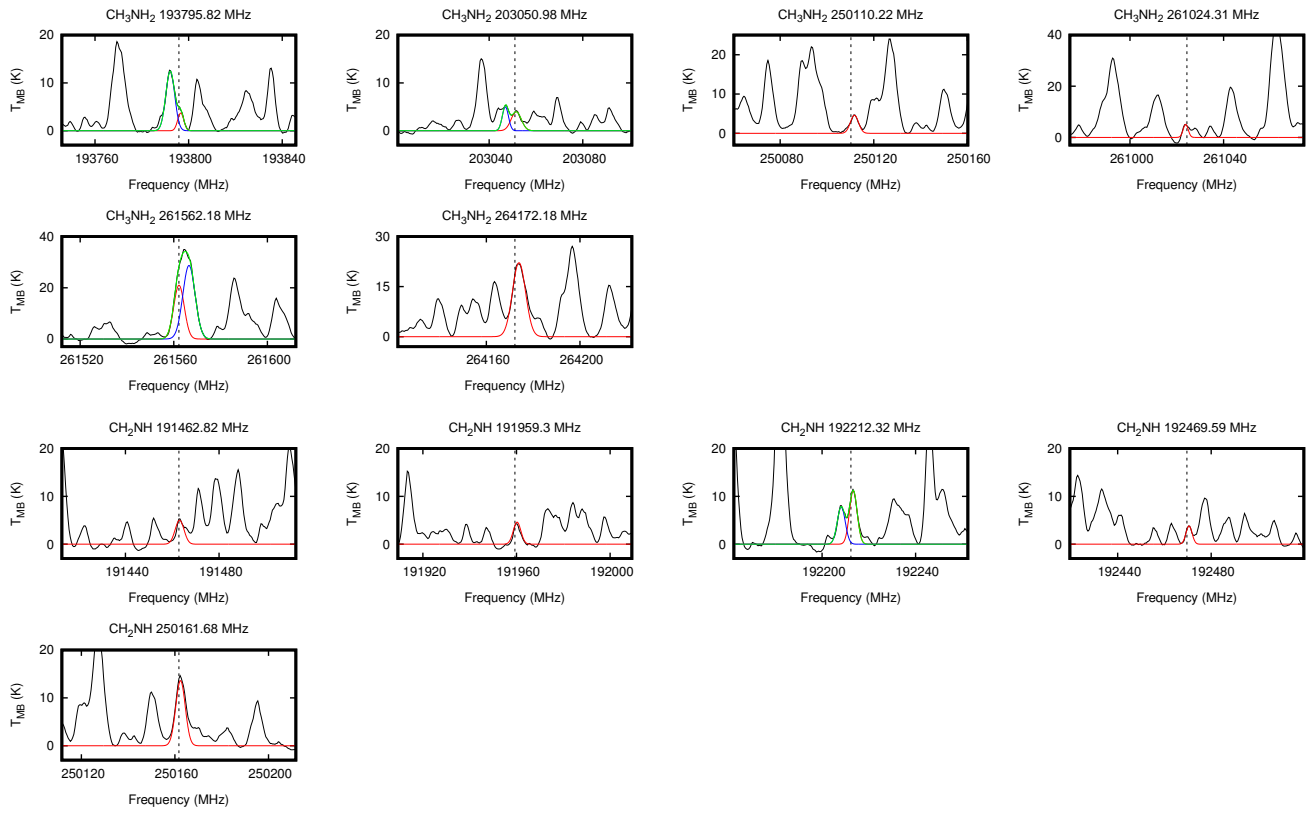


Figure 12. The same as Figure 7 but toward W51 e2.

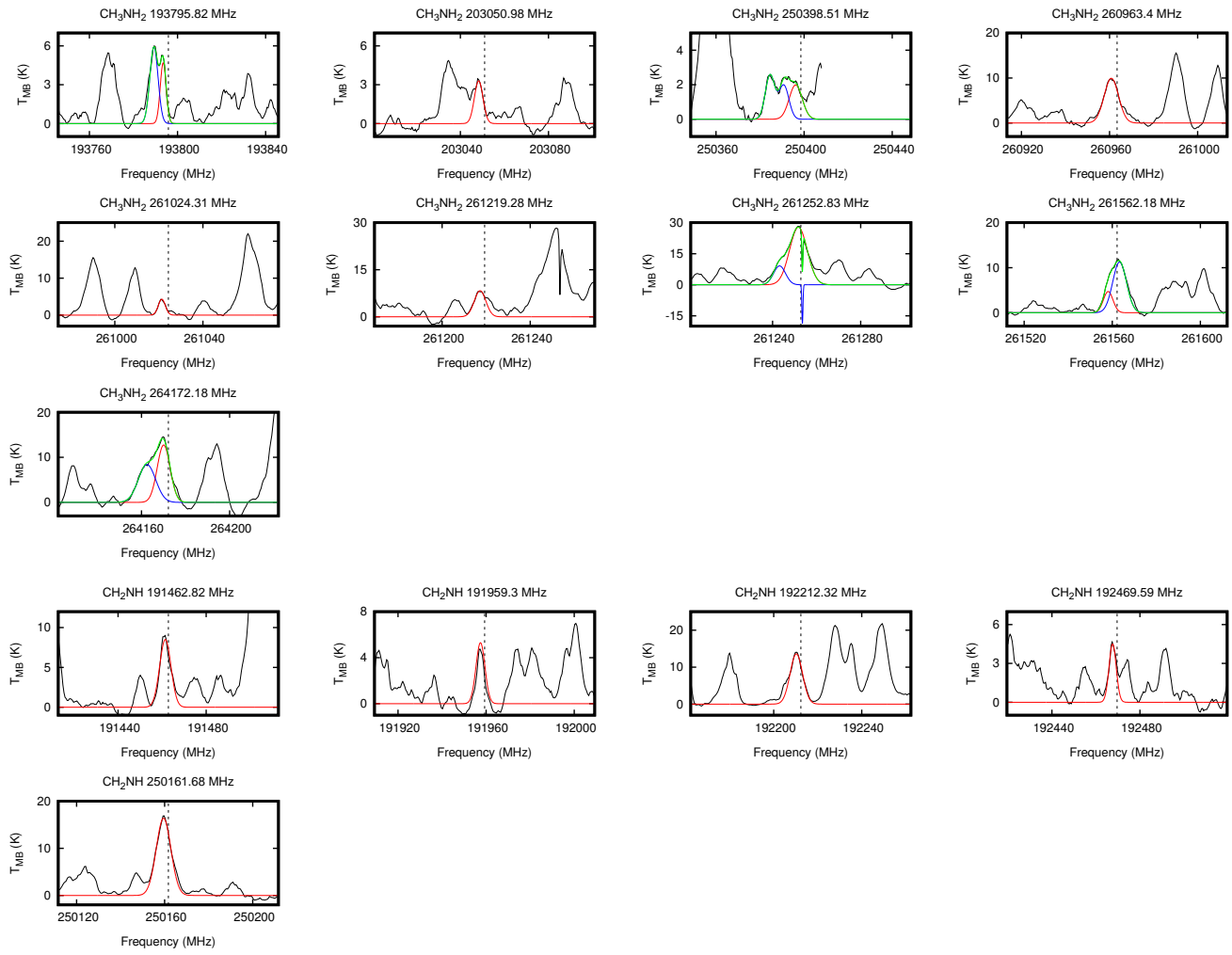


Figure 13. The same as Figure 7 but toward W51 e8.

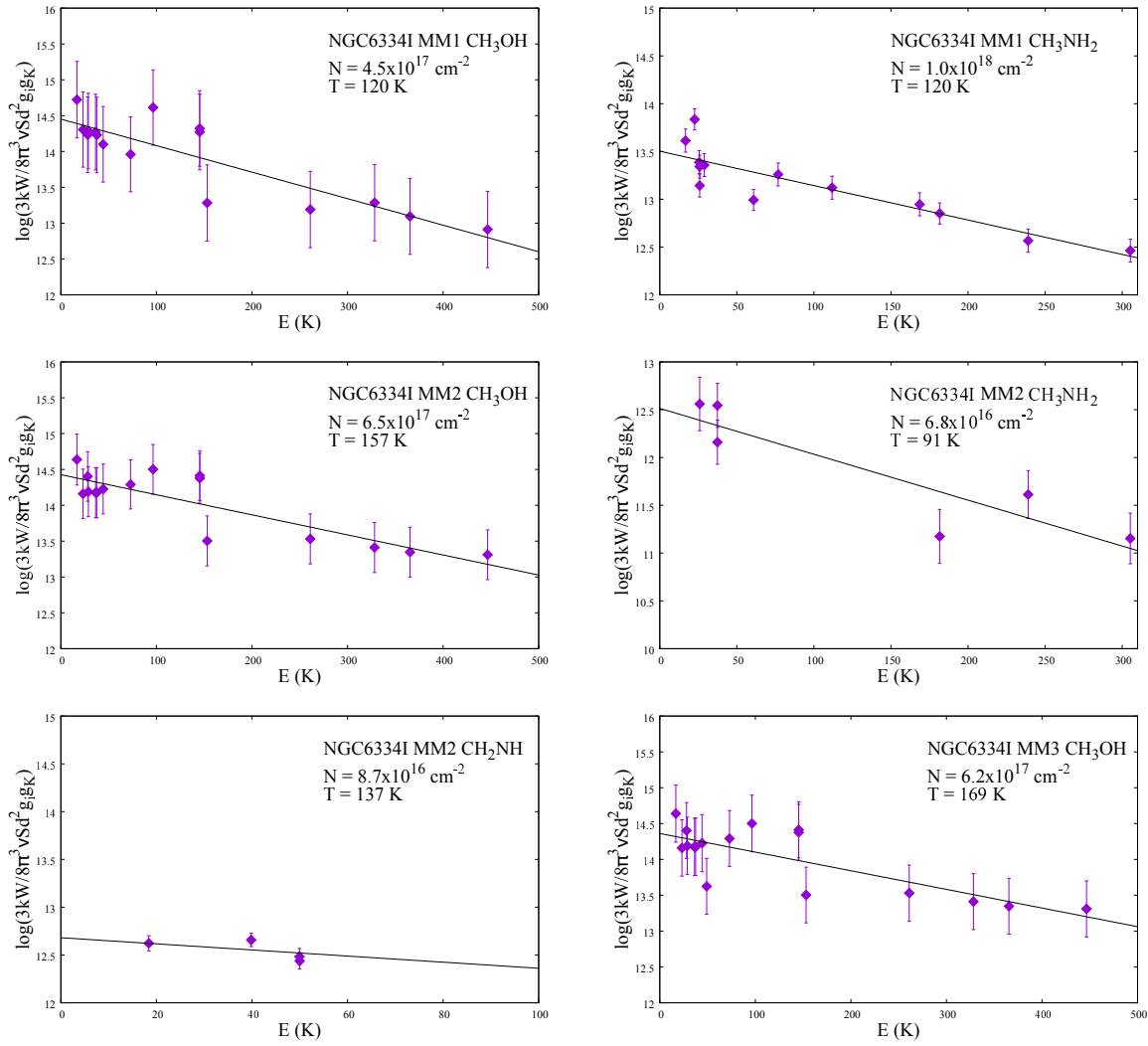


Figure 14. The rotation diagrams of CH_3OH , CH_3NH_2 , and CH_2NH for NGC6334I MM1, MM2, and MM3.

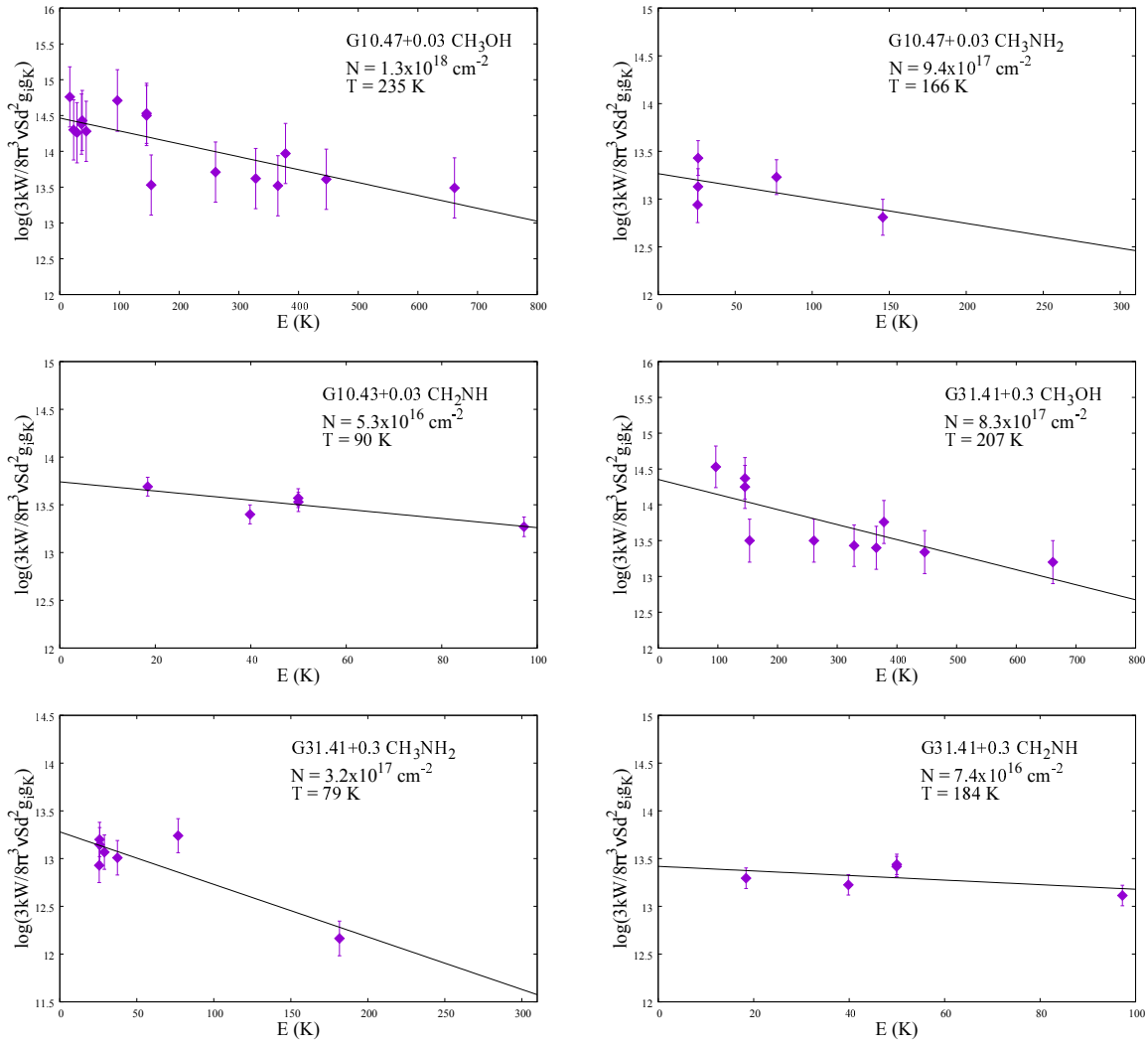


Figure 14. (continued) The rotation diagrams of CH₃OH, CH₃NH₂, and CH₂NH for G10.47+0.03 and G31.41+0.3.

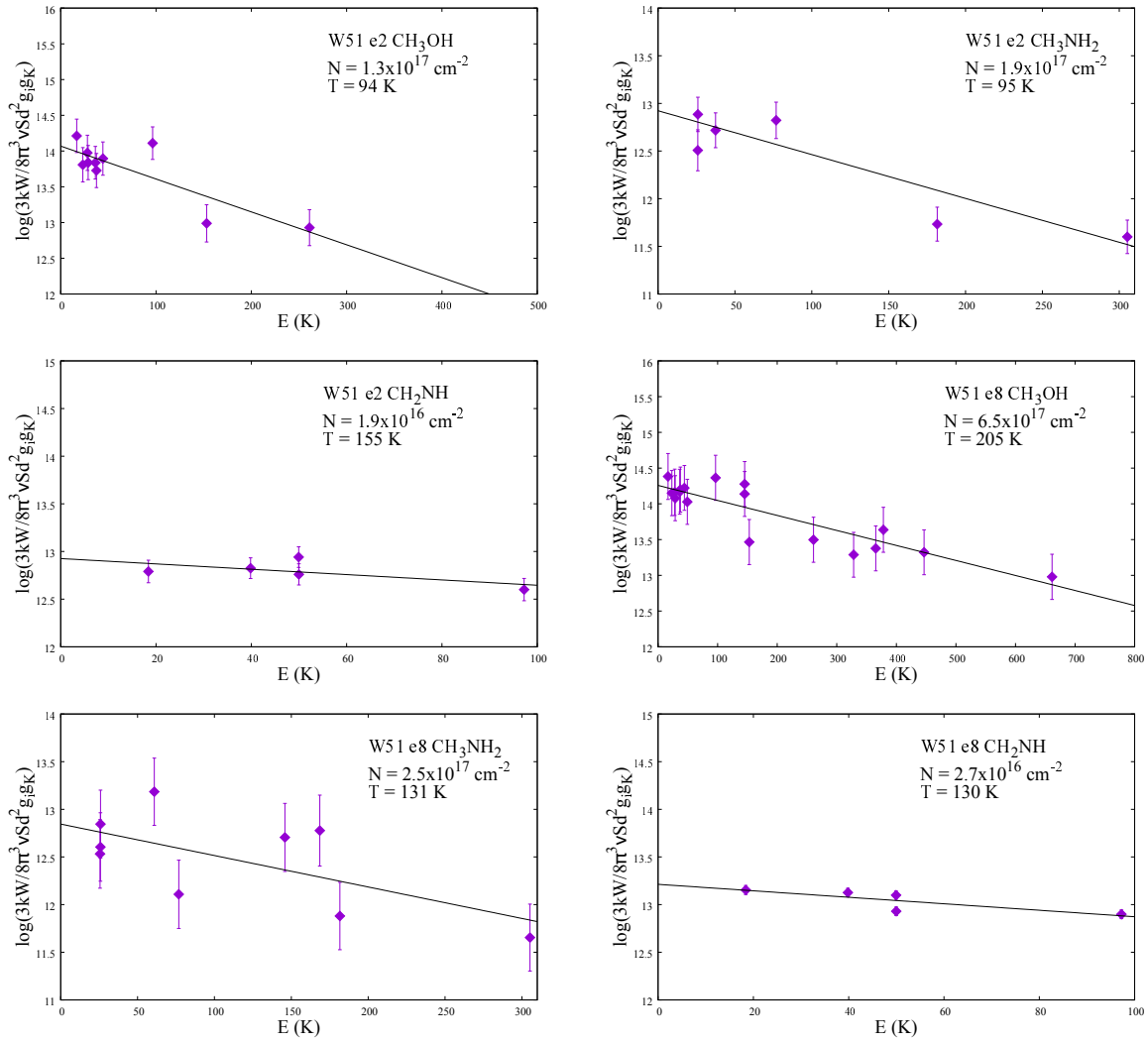


Figure 14. (continued) The rotation diagrams of CH₃OH, CH₃NH₂, and CH₂NH for W51 e2 and e8.

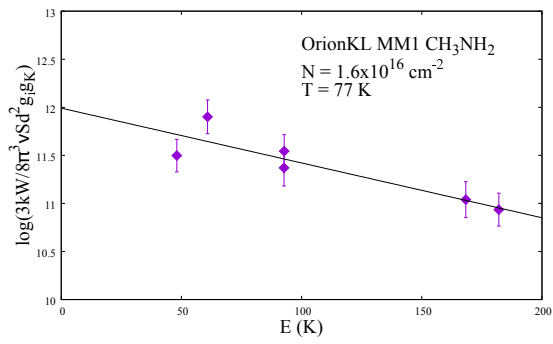


Figure 15. (continued) The rotation diagram of CH₃NH₂ for Orion KL Hot core analyzed by the archival data.

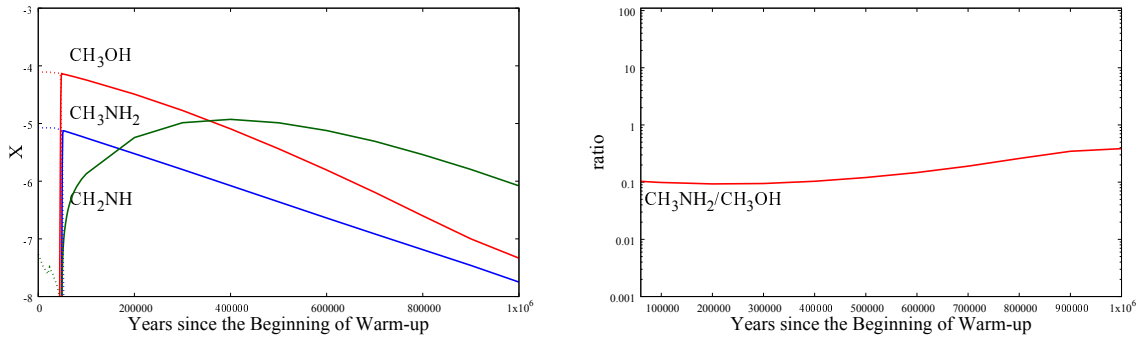


Figure 16. (Left) The simulated fractional abundance, X , for CH_3OH , CH_3NH_2 , and CH_2NH in the gas phase are shown by red, blue, and green solid lines, respectively. The dotted line represent the sum of the fractional abundances of those species in the grain mantle and on the grain surface. (Right) The gas phase molecular abundance ratios of “ $\text{CH}_3\text{NH}_2/\text{CH}_3\text{OH}$ ” and “ $\text{CH}_3\text{NH}_2/\text{CH}_2\text{NH}$ ” are shown by red and green lines, respectively.